Convection patterns in end-heated inclined enclosures

R. Delgado-Buscalioni*
Departamento de Física Fundamental, UNED, Apartado 60141, Madrid 28080, Spain
(Received 19 October 2000; published 12 June 2001)

The natural convection in inclined side-heated rectangular boxes with adiabatic walls is theoretically and numerically investigated. The study is focused on the characterization of the convection patterns arising at the core of the basic steady unicellular flow and covers the whole range of Prandtl numbers ($0 \leqslant \mathrm{Pr} \leqslant \infty$) and inclinations (from $\alpha = 0°$, heated-from-below vertical cavities, to $\alpha = 180°$). The onset of the flow instabilities depends on the core Rayleigh number $R \equiv K\,\mathrm{Ra}$, defined in terms of the local streamwise temperature gradient, $K\Delta T/L$. The critical value of R for transversal and longitudinal modes is determined by the linear stability analysis of the basic plane-parallel flow, which also provides the stability diagram in the $(\mathrm{Pr}-\alpha)$ chart. Anyhow, the effect of confinement can decisively change the stability properties of the core: if the steady unicell reaches the boundary layer regime (BLR) the local temperature gradient vanishes at the core leaving a completely stable core region. A theoretical determination of the frontier of the BLR in the space of parameters (α, R, and cavity size) yields an extra criterion of stability that has been displayed in the stability diagram. As confirmed by numerical calculations, the core-flow instabilities can only develop for $\mathrm{Pr} < O(1)$ whereas, at larger Pr the core region remains stable and the instabilities may only develop at the boundary layers. The analysis of the instability mechanisms reveals several couplings between the momentum and temperature fields that are not possible in the horizontal ($\alpha = 90°$) or vertical limits. For instance, by tilting the cavity with respect to $\alpha = 0°$, the (Rayleigh-Bérnard) stationary thermal mode is suppressed in cavities whose depth is smaller than a theoretically predicted cutoff wavelength. The inclination also alters the properties of the oscillatory longitudinal instability, extensively investigated in the horizontal Hadley configuration at low Pr (liquid metals). An analytical relationship for its frequency in terms of α, Ra, and Pr is derived. Throughout the paper, numerical calculations in two- and three-dimensional enclosures illustrate each type of multicellular flow and examples of instability interactions near the codimension-2 lines predicted by the theory.

DOI: 10.1103/PhysRevE.64.016303 PACS number(s): 47.15.Fe, 47.15.Rq, 47.20.Bp, 47.20.Ft

I. INTRODUCTION

Natural convection in slender cavities driven by imposed end-to-end temperature differences has been the subject of theoretical and experimental works since the last 30 years. Practically all the published works have considered horizontal or vertical cavities, although in most of the practical applications in both industrial and natural processes, the inclination plays a very important role. A relevant example is the process of crystal growth from melts. Recent numerical calculations on the vertical Bridgman setup have shown that experimentally unavoidable tilt angles as small as $\alpha = 0.5°$ cause nonaxisymmetric growth conditions [1]. Also, by slightly tilting the horizontal Bridgman configuration larger mass transport rates are obtained [2]. In the same manner, the heat transfer in heat exchangers and thermosiphons can be enhanced by selecting the optimum inclination, and in fact, their efficiency has been improved by using an inclined setup [3]. The relation between the inclination and the Nusselt number has also a direct interest for reducing the loss of energy in honeycomb solar collector plates. The problem of convective transport appears also in many geophysical situations occurring in mining and geological process [4]. A particular important problem in this field is the transport rate of spread of passive contaminants such as radioactive materials in long rock fractures arbitrarily inclined with respect to the gravity vector. As shown in Ref. [4], owing to the earth's inner temperature gradient, the transport of contaminants by convection is much faster than by diffusion. In any of these applications it is rather important to control the onset of multicellular or time dependent flow because it has a direct influence on the heat and mass transport rates. Practical information concerning this point is given in this paper.

Figure 1 shows the geometry of the problem and illustrates the simplest convection pattern of the system: a steady unicellular flow that comes up for any not vertical position as a response of any small enough temperature difference ΔT. The unicellular flow in the horizontal configuration (the so-called Hadley cell) impelled the largest number of theoretical and experimental papers: since the first comprehensively work by Cormack and co-workers (see [5]) to the clarifying study done by Boehrer [6]. Briefly, as the Rayleigh number

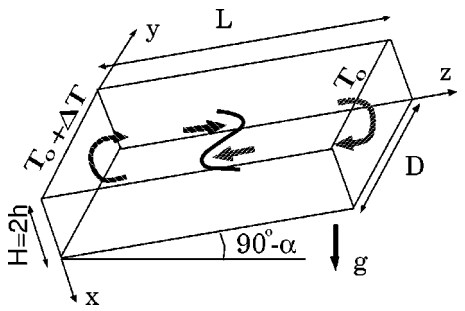

FIG. 1. The geometry of the problem and the structure of the basic unicell.

*Email address: rafa@fisfun.uned.es

increases the unicellular flow evolves from a conductive regime to a boundary layer regime in which almost all the temperature drop and the vorticity production are localized in thin layers adjacent to the end walls. The effect of the inclination on the unicellular flow has received much less attention in the past literature and one can only find empirical fits of the heat [7] or mass transfer [2] obtained from numerical calculations. The recent work presented in Ref. [8] provides a theoretical description on how the inclination modifies the structure of the steady unicellular flow and the heat transfer regimes, and presents analytical trends for the Nusselt number, maximum velocities and thickness of the boundary layers, corroborated by numerical calculations in (two-dimensional) 2D end-heated enclosures.

Although it is possible to find studies on the effect of inclination on the flow bifurcations in squared geometries (e.g., see [9] and references therein), the stability of the basic unicell in long side-heated enclosures has been hitherto considered for vertical or horizontal configurations. In a long heated-from-below vertical cavity ($\alpha=0°$) the rest solution breaks down at a certain Pr-independent critical Rayleigh number owing to a long-wavelength stationary longitudinal thermal mode whose motion occupies the whole extension of the cavity in a unique cell (see Ref. [10]). Concerning the stability of the basic flow in the horizontal configuration ($\alpha=90°$) the first experimental [11] and theoretical studies [12,13] were in part motivated by the control of time dependent flow in crystal growth process. The linear stability analysis of the basic parallel flow (see Refs. [13–15]) predicts that the stationary transversal (ST) rolls are the most dangerous ones for $\mathrm{Pr}<0.034$ whereas the oscillatory longitudinal (OL) instability dominates at larger Prandtl number, $0.034<\mathrm{Pr}<0.2$. The ST instability is driven by the mean shear stress while, as shown by Gill [12] and Hart [13], the OL instability arises as a consequence of a dynamical coupling between the mean shear stress and the buoyancy force. In a horizontal enclosure with adiabatic walls there is a sudden increase of stability for $\mathrm{Pr}>O(0.1)$, owing to the presence of a completely stable cross-stream stratification. In particular, for $\mathrm{Pr}>0.12$, the flow becomes stable to transversal modes [14–16] and although previous stability analyses of the plane-parallel flow (in unbounded domain) predicted the possible onset of stationary longitudinal short-wavelength (SL_s) rolls at least until $\mathrm{Pr}\sim 1$ [15], these rolls have not been observed in any experiment or numerical calculation on the pre-boundary-layer regime. On the contrary, for larger Prandtl number ($\mathrm{Pr}>0.2$) and $\alpha=90°$, the breakdown of the steady unicell takes place inside the boundary layers developed at larger values of Ra. As a consequence, previous experiments in horizontal cavities concerned with the investigation of core-flow instabilities worked with liquids metals ($\mathrm{Pr}\sim 10^{-2}$), whereas those interested in boundary layer instabilities used gases or liquids, with larger Pr (see [17] and references therein). It is interesting enough (see Ref. [18]) that if the cavity is inclined and heated from below ($\alpha<90°$), the stationary transversal rolls can be still observed in gases ($\mathrm{Pr}=0.7$) together with a buoyancy driven long-wavelength oscillatory transversal (OT_l) instability. These results come out from a previous study on the transversal perturbations in the 2D flow (Ref. [18]). The present paper extends the results of Ref. [18] to confined (2D and 3D) geometries and also considers the stability properties of the basic flow subject to longitudinal perturbations in terms of the inclination angle and the Prandtl number.

Owing to the great variety of instabilities revealed, the Hadley configuration was soon also thought of as a practical support for investigating the interaction between hydrodynamic instabilities and new possible routes to chaos. Numerical calculations in 2D geometries showed that if $\mathrm{Pr}<0.025$, a Hopf bifurcation follows the onset of the stationary shear rolls and also that the flow may gain in complexity by passing through several oscillatory branches (see [19] and references therein). Anyhow relatively more recent numerical calculations in 3D geometries showed that in low-Pr fluids the third dimension enables completely different scenarios to those reported in 2D (see [20,21]). In fact, around $\mathrm{Pr}\sim 0.025$ rather complex dynamics may arise because the transversal and oscillatory longitudinal rolls are triggered at relatively close values of Ra. This is a favorable situation for any experiment concerned with the characterization of new routes to chaos (see [22–24]) for which part of the endeavor consists of finding lines of the space of parameters where two different type of bifurcations intersect. In order to make this situation feasible, a required procedure is to increase the codimension space of the experimental system. This can be done via the Hartman number, i.e., by introducing a variable magnetic field perpendicular to the basic flow (see Refs. [23,24]). Alternatively, as shown in Ref. [22], it is also possible to vary the Prandtl number of the working fluid ($0.015\leqslant \mathrm{Pr}\leqslant 0.022$) to explore a region of the Pr-Gr space. As a result, in these experiments new types Hopf-Hopf interaction were reported. A third alternative is to change the inclination of the cavity. This possibility was proposed in Ref. [21], which presents numerical calculations in a 3D cavity inclined at $\alpha=80°$ and filled with a $\mathrm{Pr}=0.025$ fluid, and illustrates the underlying flow structure at the onset of the biperiodic regime. In that configuration, the onset of the oscillatory flow is due to the OL instability and the origin of the secondary frequency was shown to be a consequence of the interaction between OL rolls and a transversal wave formed by shear rolls. In the numerical calculations of Ref. [21], the choice of the inclination angle was done according to the stability results presented in this work, which predict a codimension-2 line formed by the OL and ST branches passing through that set of parameters, $(\mathrm{Pr},\alpha)=(0.025,80°)$. This paper also presents the derivation of an analytical trend for the OL frequency, which sucessfully reproduces the primary frequency reported in the numerical calculations of Ref. [21]. In summary, the results of Ref. [21] indicate that the inclined Hadley configuration can be used as a relatively simple setup to make feasible the investigation of instability interactions by a suitable choice of the inclination angle. Further examples are given in this paper.

The rest of the paper proceeds as follows. The basic steady unicellular flow is described in Sec. II, where the flow profiles at the core and the local axial temperature gradient at the core, $K\Delta T/L$, are expressed in terms of the aspect ratio, Rayleigh number, and the inclination. Section III presents

the linear stability analysis of the basic flow in terms of the local Rayleigh number at the core $R=K\,\mathrm{Ra}$. The map of instabilities in the α-Pr chart is then constructed. The rest of the paper (Secs. IV–VIII) is devoted to each flow instability, discussing the mechanisms underlying each type of perturbation and the effect of confinement. Throughout Secs. IV–VIII, flow calculations in 2D and 3D cavities, based on the numerical methods presented in the Appendix, illustrate each type of multicellular flow and some examples of interaction between instabilities. Conclusions are given in the last section.

II. UNICELLULAR FLOW

Let us consider the flow in the cavity of Fig. 1. The dimensions of the cavity along x, y, and z directions (width, depth, and length) are, respectively, $H=2h$, D, and L. The z axis is inclined an angle α with respect to the gravity vector $\mathbf{g}=g\mathbf{e}_g$ with $\mathbf{e}_g=\sin(\alpha)\mathbf{i}-\cos(\alpha)\mathbf{k}$, and a temperature difference ΔT is imposed between the $z=\{0,L\}$ walls. An incompressible fluid with thermal expansion coefficient β, kinematic viscosity ν, and thermal diffusivity κ, fills the cavity and its motion is governed by the Navier-Stokes and heat transport equations with the Boussinesq approximation. The boundary conditions correspond to adiabatic rigid walls (nonslip assumed). The governing equations [Eqs. (A1)–(A3)] and boundary conditions [Eqs. (A4)–(A6)] are shown in the Appendix and have been nondimensionalized by using h, h^2/ν, $g\beta\Delta T h^3/L\nu$, ΔT, and $\rho_o g\beta\Delta T h^2/L$ as scales of length, time, velocity, temperature, and pressure. The dimensionless parameters are the inclination angle α, the aspect ratios $A_z=H/L$ and $A_y=H/D$, the Rayleigh number $\mathrm{Ra}=g\beta\Delta T h^4/L\nu\kappa$, and the Prandtl number $\mathrm{Pr}=\nu/\kappa$.

For any not vertical position the mechanical equilibrium is not possible and any externally imposed temperature difference leads to a clockwise cellular flow whose simplest form is illustrated in Fig. 1 in a cavity with $A_z<1$. The flow at the core region is nearly plane-parallel and turns around at the end regions, at a distance of order $O(A_z)$ adjacent to the $z=\{0,2A_z^{-1}\}$ walls. The lateral walls at $y=\pm A_y^{-1}$ impose an even modulation in the flow amplitude, which is only relevant at diffusive layers of thickness $O(A_y)$ [see Fig. 8(a), below]. As discussed in Ref. [25], in wide enough cavities ($A_y<1$) and away from these layers, one can neglect the flow y dependence and describe the basic circulation as a two-dimensional steady flow in the XZ plane governed by the equation for the y component of vorticity ($\omega_y=\partial u/\partial z-\partial w/\partial x$) and the heat equation,

$$\frac{\partial\omega_y}{\partial t}+\mathrm{Ra}\,\mathrm{Pr}^{-1}\mathbf{v}\cdot\boldsymbol{\nabla}\omega_y=\nabla^2\omega_y-\frac{2}{A_z}\left(\cos\alpha\frac{\partial T}{\partial x}+\sin\alpha\frac{\partial T}{\partial z}\right), \tag{1}$$

$$\mathrm{Pr}\frac{\partial T}{\partial t}+\mathrm{Ra}\left(u\frac{\partial T}{\partial x}+w\frac{\partial T}{\partial z}\right)=\nabla^2 T. \tag{2}$$

At the core region we assume that the flow can be described by a plane-parallel solution whose structure at the steady state is the following:

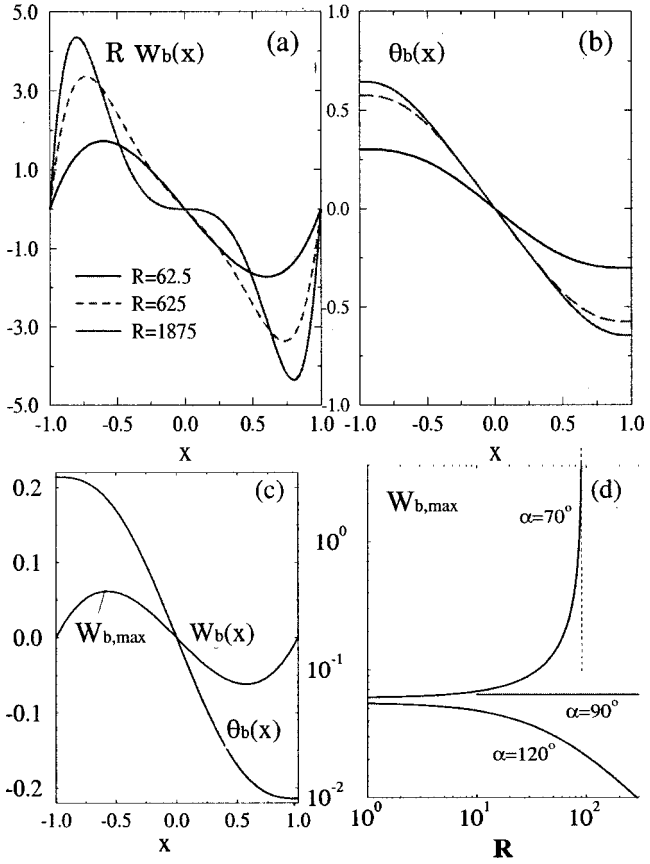

FIG. 2. (a) Basic velocity (in units of κ/h^2) and (b) temperature profiles (in units of $K\Delta T h/L$) for $\alpha=120°$ at several values of R. (c) Flow profiles for $\alpha=50°$ and $R=10$ and (d) the maximum value of $w_b(x)$ (in units of $R\kappa/h$) against R.

$$\mathbf{v}=Kw_b(x)\mathbf{k},\quad T=\frac{KA_z}{2}[z+\theta_b(x)+b], \tag{3}$$

where K is the ratio between the streamwise temperature gradient at the core and the externally imposed temperature gradient. The validity of Eq. (3) is analyzed afterwards. By substituting Eq. (3) into Eqs. (1), (2) and considering the boundary conditions [Eqs. (A4)–(A6)], one obtains a system of ordinary equations for the velocity and temperature profiles at the core, $w_b(x)$ and $\theta_b(x)$. For a fixed angle, the shape and intensity of the basic profiles are governed by the local Rayleigh number at the core, $R\equiv K\,\mathrm{Ra}$, and the functional form of the analytical solutions is: $w_b=\sin\alpha f(x;R\cos\alpha)$ and $\theta_b=\sin\alpha g(x;R\cos\alpha)$. The interested reader is referred to [8] for the explicit analytical expressions of the core-flow profiles at arbitrary α. The evolution of the flow profiles with the Rayleigh number (see Fig. 2) is ruled by the balance of dissipation and production of vorticity by buoyant forces. At low values of Ra, in the conducting regime the cross-stream temperature gradient is vanishingly small and the vorticity is generated by the cross-stream component of gravity, at a rate given by $\sin\alpha\partial T/\partial z$ [see Eq. (1)]. This induces a clockwise cellular flow whose x dependence coincides with the Hadley profile for $\alpha=90°$: $w_b(x)=\sin\alpha(x^3-x)/6$ and $\theta_b(x)=-\sin\alpha(x^5/120-x^3/36+x/24)$.

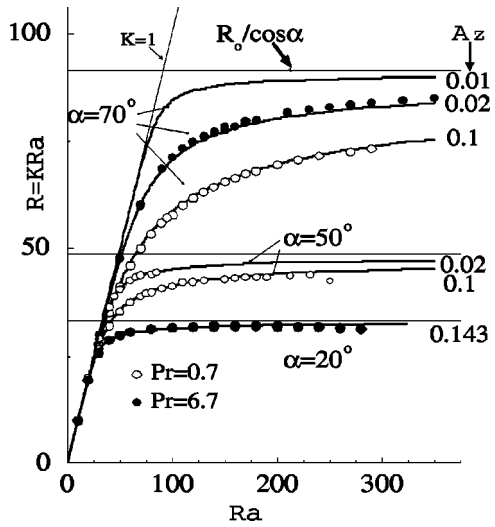

FIG. 3. The local Rayleigh number at the core, $R=K$ Ra, versus the external Rayleigh number Ra. Circles corresponds to the numerical solution of the flow at several values of Pr and lines to the theoretical model.

As Ra increases the streamwise advection creates an increasing (negative) temperature gradient along the x axis, which acts as another source of motion owing to the presence of the streamwise component of buoyancy. As shown in Eq. (1), this term produces vorticity at a rate given by $\cos\alpha\partial T/\partial x$ and hence its effect greatly depends on the range of the inclination angle. If the cavity is heated from above ($\alpha>90°$), both terms, $\cos\alpha\partial T/\partial x$ and $\sin\alpha\partial T/\partial z$, have opposite signs meaning that the streamwise buoyant force tends to reduce the convection. As seen in Fig. 2(a), this reduction occurs mostly around the center of the layer where $\partial T/\partial x$ is larger. On the contrary, if the cavity is heated from below ($\alpha<90°$), both sources of vorticity have the same sign and as Ra increases a positive feedback loop between $w_b(x)$ and $\theta_b(x)$ occurs: any increment of the flow intensity increases the cross-stream temperature gradient, which in turn, enhances the intensity of the clockwise flow. A consequence of this feedback coupling is that the analytical solution for w_b and θ_b diverges at a discrete set of values of $R\cos\alpha$, the lowest one being $R_0 \simeq 31.285$ [see Fig. 2(d)].

In order to understand how the divergence of the plane-parallel flow analytical solution affects the behavior of the total flow, one has to consider the effect of confinement by matching the flow at the core with the flow at the end regions. This task have been solved by using an integral method similar that of Bejan and Tien [26], which yields the value of K in terms of Ra, α, and A_z. This calculation provides the proper increase rate of the flow intensity in terms of the externally imposed Rayleigh number Ra and, as discussed in Ref. [8], valuable information concerning the flow and heat transfer regimes of the unicellular flow. Here we are interested in the relation of the governing core-flow parameter, $R=K$ Ra with the external parameters (Ra, α, A_z), which is illustrated in Fig. 3. The first important conclusion arising from Fig. 3 is that, for any $\alpha<90°$ or any $A_z<1$, the value of the local Rayleigh number at the core R is bounded and tends asymptotically to $R_0/\cos\alpha$. On the contrary, for $\alpha>90°$, K reaches a minimum and tends to 1 at large Ra [8], thus when heating from above, $R\simeq$Ra. In conclusion, the domain of values of R to be considered in the stability analysis of the core flow is $R>0$ for $\alpha\geqslant 90°$ or $\alpha=0°$ and $0<R<R_0/\cos\alpha$ for $\alpha<90°$. Note in passing that although an upper limit for R is also to be found in other configurations with two components of buoyancy, this fact was not taken into account in previous works [10,4], which therefore reported unphysical divergences of mean flow properties at several values of the Rayleigh number. Also, the existence of an upper bound for R is related to an important difference between the inclined ($\alpha<90°$) and horizontal configurations. For $\alpha=90°$ the conducting regime ($K\approx 1$) holds for $\mathrm{Ra}<6.25A_z^{-1}$ [26], so in large cavities ($A_z\ll 1$), the equality $R\simeq$Ra stands until very large values of Ra. As seen in Fig. 3, for $\alpha<90°$ this conclusion is no longer valid because, regardless of the size of the cavity, K largely differs from 1 once the transition regime is established at $\mathrm{Ra}>R_0/\cos\alpha$. In summary, for $\alpha<90°$ a careful evaluation of $R=R(\mathrm{Ra},A_z,\alpha)$ is required in order to apply the stability predictions at the core (given in terms on R) to any realistic closed configuration.

The solution derived from Eq. (3) is strictly valid at the core of a infinity long and wide cavity ($A_z\to 0$, $A_y\to 0$) (see Ref. [5]). In a finite cavity the flow at the core can be described by Eq. (3) while it is possible to neglect the inertial terms in the momentum equation and the cross-stream advection in the heat equation (i.e., $u\partial T/\partial x\ll w\partial T/\partial z$). As shown in Ref. [8], both conditions are satisfied in the conducting and transition regimes but fail at large Ra, in the boundary layer regime. In the boundary layer regime BLR the isothermals at the core region are almost parallel to the z axis ($\nabla^2 T\simeq 0$) and although at the core $u\ll w$ the balance of heat flux yields $u\partial T/\partial x\sim -w\partial T/\partial z$ for any $\alpha<90°$. The BLR appears only if $\alpha\leqslant 90°$: at $\mathrm{Ra}>625A_z^{-1}$ for $\alpha=90°$ [6] and at $\mathrm{Ra}>10R_0/\cos\alpha$ for $\alpha<90°$ [8]. We refer to Ref. [8] for a description of the BLR in the tilted geometry.

III. LINEAR STABILITY ANALYSIS

In order to study the stability of the flow at the core region, it is convenient to use the proper local temperature z gradient at the core $K\Delta T/L$ in the temperature scaling. By doing this the scale of temperature in the perturbation equations is $(K\Delta T/L)h$ and the basic velocity and temperature fields are $\mathbf{v}=w_b(x)\mathbf{k}$ and $T_b=-z+\theta_b(x)$. The linearized equations for the perturbative flow are obtained in the usual way: inserting each flow variable as the sum of the mean flow quantity and a small perturbation into Eqs. (A1)–(A3) and neglecting products of perturbative quantities. At this stage of the analysis, the modulation of the basic flow in the z and y directions shall not be taken into account and the perturbative quantities can be expressed as normal modes,

$$\{\mathbf{v}_p,T_p,P_p\}=\{\mathbf{v}(x),\theta(x),p(x)\}\exp(imy+ikz+\lambda t). \tag{4}$$

The subscript ''p'' refers to perturbation quantities, m and k are real wave numbers and $\lambda=\lambda_r+i\lambda_i$ is the complex

TABLE I. Trends of the critical parameters of each type of instability. Those given for the SL_s and OL instabilities corresponds to $\alpha=90°$ and fit to the linear stability results within deviations of about 2%. (See Sec. III A for nomenclature.)

	Critical R	Critical wave no.	Critical frequency
ST	$\mathrm{Pr}\ll 1,\ R_{ST}\simeq 495\,\mathrm{Pr}/\sin\alpha$	$k_{ST}\simeq 1.35$	0
	$\mathrm{Pr}\sim 1\ (\alpha<90°),\ R_{ST}\simeq R_0/\cos\alpha$	$k_{ST}\simeq 1.6$	0
OT_l	$R_{OT_l}\simeq R_0/\cos\alpha$	$k_{OT_l}\sim 0.3$	$f_{OT_l}\simeq 0.91\left(1-\frac{0.08}{\mathrm{Pr}}\right)w_{b,\max}$
SL_l	$R_{SL_l}=0$	$m_{SL_l}=0$	0
SL_s	$R_{Sl_s}\simeq \frac{1160\,\mathrm{Pr}^{1/2}}{(0.8-\mathrm{Pr})^2}$	$m_{SL_s}\simeq 2.9$	0
OL	$R_{OL}\simeq \frac{47.27\,\mathrm{Pr}^{1/2}}{(0.21-\mathrm{Pr})^{1/2}}$	$m_{OL}\simeq \frac{(0.21-\mathrm{Pr})^{0.4}}{0.25\,\mathrm{Pr}^{-1/2}}$	$f_{OL}\simeq \frac{1.24}{(0.21-\mathrm{Pr})^{0.1}}\frac{\nu}{h^2}$

growth rate. As shown by Laure and Roux [14] and Kuo and Korpela [15], oblique perturbations $(k,m\neq 0)$ do not appear in the horizontal case and we have not found this type of perturbations in the inclined geometry. Therefore we shall focus our attention on longitudinal $(k=0)$ and transversal $(m=0)$ modes.

The transversal perturbations are independent of the y coordinate and are essentially bidimensional modes. Its flow can be described by a perturbative stream function $\Psi(x,z,t)=\varphi(x)\exp(ikz+\lambda t)$, which satisfies $u_p=\partial\Psi_p/\partial z$, $w_p=-\partial\Psi_p/\partial x$. By taking the curl in the equation of perturbative momentum and substituting Eq. (4) in the resulting equation one obtains

$$\lambda\nabla^2\varphi=\nabla^4\varphi-ik\,\mathrm{Gr}(w_b\nabla^2\varphi-w_b''\varphi)-[\cos(\alpha)\theta'+ik\sin(\alpha)\theta], \tag{5}$$

$$\mathrm{Pr}\,\lambda\,\theta=\nabla^2\theta-R(ik\theta_b'\varphi+\varphi'+ikw_b\theta), \tag{6}$$

$$\varphi=\varphi'=\theta'=0 \quad \text{at } x=\pm 1. \tag{7}$$

The longitudinal perturbations are helicoidal modes whose motion can be represented by the perturbative velocity along the z axis and a perturbative stream function $\Phi_p(x,y,t)=\psi(x)\exp(imy+\lambda t)$ that describes the flow in the XY plane ($u_p=-\partial\Phi_p/\partial y$ and $v_p=-\partial\Phi/\partial x$). The equations for the amplitude of longitudinal perturbations are

$$\lambda w=\nabla^2 w+imRPr^{-1}w_b'\psi+\cos(\alpha)\theta, \tag{8}$$

$$\lambda\nabla^2\psi=\nabla^4\psi+im\sin(\alpha)\theta, \tag{9}$$

$$\mathrm{Pr}\ \lambda\,\theta=\nabla^2\theta+R(w+im\theta_b'\psi), \tag{10}$$

$$\psi=\psi'=\theta'=0 \quad at\ \ x=\pm 1, \tag{11}$$

where in Eqs. (8) and (9) the pressure has been eliminated by cross derivation in the x and y projections of the perturbative momentum equation.

The eigenvalue problems for both transversal [Eqs. (5)–(7)] and longitudinal perturbations [Eqs. (8)–(11)] have been solved by a Tau-Chebyshev method. The number of basis functions for the amplitude of velocity and temperature perturbations N was chosen to preserve accuracies (in eigenvalue and eigenfunction) of less than 1% and typically varied from $N=15$ for low Pr to $N=25$ for large Pr and α. At the minima of each branch of the neutral curve (determined by $\lambda_r=0$) one obtains the critical parameters (R and wave number) and the critical frequency (from the corresponding value of λ_i). Our stability results have been validated by comparison with those reported by Laure and Roux [14] and Kuo and Korpela [15] for $\alpha=90°$. Differences of less than 2% in the critical Rayleigh number, wave number, and frequency are found in the worst cases.

A. Nomenclature and type of instabilities

Table I shows the trends of the critical parameters of the several instabilities found for $0\leqslant\mathrm{Pr}\leqslant\infty$ and $0°\leqslant\alpha\leqslant 180°$. The nomenclature used for labeling each instability has two subsequent capital letters that, respectively, describe the temporal and spatial behavior of its associated perturbations: *O*, oscillatory ($|\lambda_i|>0$) or *S*, stationary ($\lambda_i=0$) and *L*, longitudinal ($k=0$) or *T*, transversal ($m=0$). In some cases an extra (lowercase) label is needed to distinguish between perturbations with *short* (*s*) or *long* (*l*) wavelength compared to the width of the cavity, $2h$.

The stability diagram of Fig. 4 indicates with bold letters, the instability with the lowest critical Rayleigh number in each region in the Pr-α chart. Those with the second lowest critical Rayleigh number are noted in italics and between parenthesis. This diagram shows also information concerning the onset of the boundary layer regime. As shown below, in the BLR the structure of the unicell changes in such a way that the core region remains stable and the instabilities may only develop at the boundary layers and at relatively large values of Ra (see Ref. [25]). Therefore, if for a set of α, Pr, and A_z, the BLR takes place at $R=R_{BLR}$ the core-flow shall be stable to a certain type of instability if its critical Rayleigh

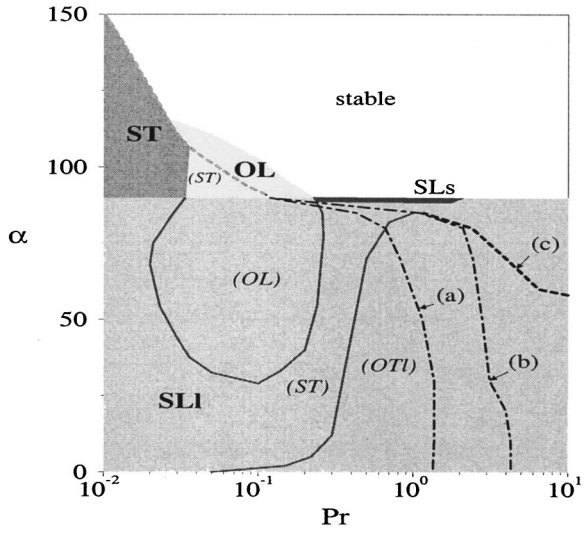

FIG. 4. The stability diagram. The instability with the lowest critical Rayleigh number is indicated with bold letters and that with the second lowest critical R is labeled in italics and between parenthesis (see Sec. III A for nomenclature). The lines noted by (a) and (b) are placed at $R_{BLR}=R_{ST}$, with R_{BLR} calculated (a) for $A_z=1/10$ and (b) for $A_z=1/50$. Line (c) corresponds to $R_{BLR}=R_{\mathrm{OT}_l}$ for $A_z=1/50$. For Pr larger than the locus of (a), (b), or (c), the core region is stable to the indicated type of instability.

number (say R_{crit}) is such that $R_{crit}>R_{BLR}$. The dashed lines in the stability diagram of Fig. 4 show the locus of this stability criterion (with ''$crit$'' standing for the ST and OT_l instabilities) in cavities with several aspect ratios. The value of R_{BLR} is directly obtained from Ra_{BLR} (given in Ref. [8]): the BLR holds for $K<0.1$ [26,8], hence $R_{BLR}=0.1\,\mathrm{Ra}_{BLR}$. Figure 5 shows the group $R_{BLR}\cos\alpha/R_0$ versus α for several values of A_z.

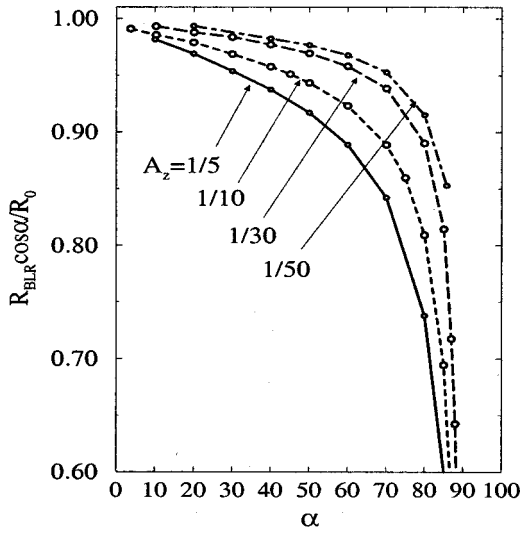

FIG. 5. The local core Rayleigh number at the onset of the boundary layer regime (R_{BLR}) scaled with $R_0/\cos(\alpha)$ ($R_0=31.285$).

B. The vertical unstable configuration, $\alpha=0°$

Some comments on the unstable vertical configuration are needed before presenting the general inclined case. For $\alpha=0°$, the basic state is the purely conductive rest solution whose stability was studied by Gershuni and Zhukhovitskii [10]. Convection takes place if the unstable temperature stratification exceeds a critical Pr-independent value that depends on the aspect ratios and the thermal boundary conditions. In the limit $A_z\to 0$ and $A_y\to 0$ (vertical parallel plates), the stability problem has an exact analytical solution [10]. For both transversal and longitudinal perturbations, the marginal Rayleigh number increases monotonically with the wave number and the critical modes have a vanishing wave number (plane parallel disturbances). In the case of adiabatic walls and for transversal and longitudinal modes, the critical Rayleigh numbers are $R_0^{tr}=31.285$ and $R_0^{lon}=0$, respectively. In our notation, the longitudinal mode for $\alpha=0°$ corresponds to the stationary longitudinal long-wavelength (SL_l) instability, hence $R_{SLl}(0°)=0$. In finite cavities with $A_z<1$, the critical Rayleigh number increases approximately like A_y^4, due to the diffusion at the lateral walls [25]. The flow associated with the longitudinal long-wavelength mode in a vertical cavity with $A_z<1$ resembles that illustrated in Fig. 8(b). It consists of a unicell that flows in the YZ plane and fills the whole extension of the cavity.

IV. THE STATIONARY LONGITUDINAL LONG-WAVELENGTH INSTABILITY (SL_L)

The SL_l instability appears for any $\alpha<90°$ and has essentially the same origin as the critical mode of the unstable vertical configuration. This is clearly revealed in the values of the critical Rayleigh number and critical wave number: $R_{\mathrm{SL}_l}(\alpha)=0$ and $m_{\mathrm{SL}_l}(\alpha)=0$. In fact, a general relationship valid for any type of thermal boundary conditions is $R_{\mathrm{SL}_l}(\alpha)=R_{\mathrm{SL}_l}(0°)/\cos\alpha$ (see Ref. [25]) meaning that the onset of the SL_l perturbation occurs once the vertical projection of the temperature stratification, $\cos\alpha\Delta T/L$, reaches the same critical value for the vertical configuration. In the particular case of adiabatic walls ($R_{\mathrm{SL}_l}=0$) the critical Rayleigh number for the SL_l instability is the lowest one for any heated-from-below configuration (see Fig. 4). In view of this result, our first impression was that for any $\alpha<90°$, the SL_l perturbation would soon be superposed onto the basic cell thus making it impossible or very difficult to observe the rest of the predicted instabilities in 3D inclined cavities. Nevertheless, as shown in the neutral curves of Fig. 6(a), there is an important difference between the inclined and the vertical configurations. In a vertical cavity, any SL_l modes with arbitrary wave number m can become unstable provided a large enough value of R. But if the cavity is inclined, the SL_l instability presents a cutoff wave number such that perturbations with $m>m_{CUT}$ are damped. The value of m_{CUT} is shown in Fig. 6(b) against α and Pr. By increasing α or decreasing Pr, the flow becomes stable to SL_l perturbations with larger wavelengths. This result suggests the possibility of filtering the SL_l instability in closed tilted 3D cavities by choosing a depth D, smaller than the cutoff wavelength,

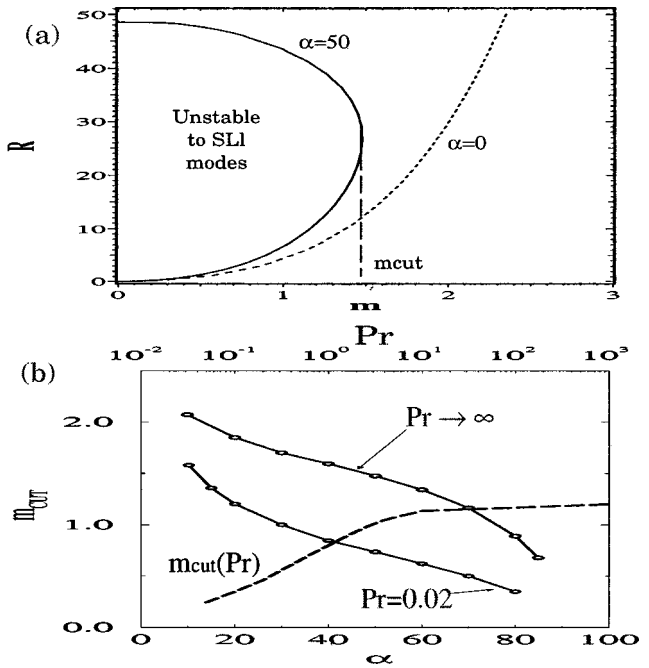

FIG. 6. (a) Neutral curve for SL_l perturbations for $\alpha=0°$ and $\alpha=50°$, Pr$\to\infty$. (b) The cutoff wave number m_{CUT} versus α (botom axis) and versus Pr for $\alpha=70°$ (upper axis).

$2\pi h/m_{CUT}$ (i.e., $A_y\pi>m_{CUT}$). This possibility was confirmed by numerical calculations presented soon afterwards.

Let us first explain how the inclined geometry enables the suppression of SL_l perturbations. The SL_l-flow is schematically represented in Fig. 7. Most part of the perturbative current is driven by the streamwise component of the buoyant force and consists of a unique cell that flows in the YZ plane filling the whole extension of the cavity. This current converts the potential energy stored in the perturbative temperature field (shown in Fig. 7 by different shading) into kinetic energy at a rate given by[1] $\cos\alpha\langle w_pT_p\rangle$. If the cavity is inclined, the temperature variation along the XY plane induces also a cross-stream flow (illustrated with solid lines in Fig. 7), which obtains kinetic energy via the x component of buoyancy at a rate given by $\sin\alpha\langle u_pT_p\rangle$. Owing to the mean stable stratification along the x axis, the cross-stream flow reduces the buoyant excess that drives the perturbation, as revealed in a negative rate of production of temperature variance, $\langle u_pT_p\theta_b'\rangle<0$. As α increases, the mean stable stratification increases ($\theta_b'\sim\sin\alpha$) and the streamwise buoyant force decreases so SL_l perturbations with longer wavelength are damped. This stabilizing mechanism has a thermal origin and is dominant at large or moderate Pr. At low Prandtl number the stabilization has a hydrodynamic origin, the Reynolds energy is negative ($-R\,\mathrm{Pr}^{-1}\langle u_pw_pw_b'\rangle<0$) meaning that in its motion along the x direction, the perturbation

[1]The operator $\langle\cdot\rangle$ denotes the average along the x direction for one wavelength. For a derivation of the balance equations for the perturbative kinetic energy and temperature variance see Refs. [15,18].

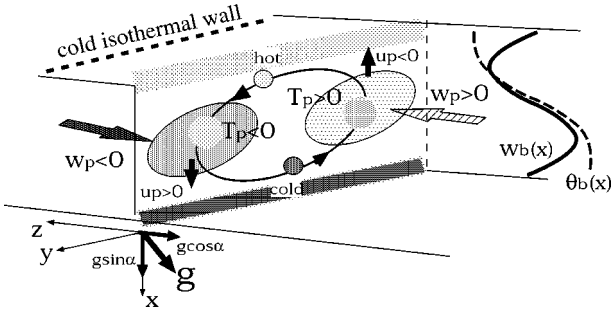

FIG. 7. Schematic view of the perturbative motion originated by the SL_l instability. The arrows indicates the sense of the perturbative flow. Darker shading corresponds to colder regions and vice versa.

works against the mean shear stress. This fact explains that for Pr<1, m_{CUT} decreases with Pr as seen in Fig. 6(b).

1. Numerical calculations

Several numerical calculations of the flow in closed 3D cavities were carried out to confirm the possibility of filtering the SL_l instability. Table II summarizes the results. In these calculations, Ra was increased up to or near the boundary layer regime in order to be sure of the stability properties at the core. As seen in Table II, the SL_l instability did not appeared in any of the configurations that satisfied the stability criteria, $A_y\pi>m_{CUT}$, while it developed in the other cases. This result confirms that the condition $A_y\pi>m_{CUT}$ yields the appropriate value of A_y to inhibit SL_l perturbations. A particularly interesting case corresponds to the set Pr$=6.7$, $A_y=2/3$, $A_z=1/10$, $\alpha=20°$, for which πA_y is quite close to m_{CUT} (see Table II). Two sets of calculations were carried out, differing in the interval of Ra between consecutive runs, Δ Ra. Using the above-mentioned set of parameters and Δ Ra$=10$, the flow became unstable for the SL_l instability whereas for Δ Ra$=50$, it maintained the basic unicellular flow and reached the BLR at large Ra. This may indicate that for $A_y\simeq m_{CUT}/\pi$, the SL_l flow coexists with the basic unicell in the space of stable solutions. A future investigation by means of a continuation technique in the space of parameters is planned to determine the branches of solutions and their stability in cavities with $A_y\sim m_{CUT}/\pi$.

Figure 8 illustrates the flow induced by the SL_l instability and its further evolution in a configuration with Pr$=6.7$, $\alpha=20°$ and $A_z=1/7$, $A_y=1/3$. The snapshots corresponds to calculations done with a mesh of $15\times35\times45$ and a time step $10^{-3}h^2/\nu$. Concerning the accuracy, variations of less than 6% are found in the velocity and temperature fields when comparing with calculations done with a double number of calculation cells in the y or z direction. At Ra$=25$ we observed the onset of the fundamental SL_l mode formed by a unique cell in the YZ section [Fig. 8(b)]. The perturbative circulation on the XY plane is shown in Fig. 8(d). At Ra $=30$ a secondary (stationary) mode composed by two pairs of counter-rotating cells in the YZ plane is superposed to the primary mode giving a flow illustrated in Fig. 8(c).

TABLE II. Details of the primary instability encountered in 3D numerical calculations. The range of Ra for the first transition is noted by $Ra^{(1st)}$. The number of longitudinal and transversal perturbative cells at the core region, n_y and n_z, respectively, and the cutoff wavelength for SL_l disturbances, π/m_{CUT}, are also indicated.

		Configuration			Details of multicellular flow		
Pr	α	A_z^{-1}	A_y^{-1}	π/m_{CUT}	Flow type	$Ra^{(1st)}$	n_y, n_z
0.05	10	10	1	2.09	ST	(45,50]	0, 2
0.025	80	4	6	8.97	ST+OL	(40,46]	3, 1
0.7	70	10	4	3.14	SL_l	(90,100]	1, 0
0.7	70	10	2	3.14	unicell		0, 0
0.7	70	10	1	3.14	unicell		0, 0
6.7	20	7	1.5	1.74	unicell/SL_l	-/(40,50]	0, 0/1, 0[a]
6.7	20	7	3	1.74	SL_l	(20,25]	1, 0

[a]The flow is conditionally unstable to SL_l disturbances and the resulting flow depends on the heating rate (see text).

V. THE STATIONARY TRANSVERSAL INSTABILITY (ST)

The ST instability takes most part of its kinetic energy from the mean shear stress and therefore in the previous studies for the horizontal case (see, for instance, Refs. [13–15]), it has been usually called ''shear instability.'' Nevertheless, if two components of buoyancy exist, the ST perturbations can obtain a large amount of its kinetic energy from the thermal field as shall be discussed below (see also Ref. [18]).

Let us first discuss the hydrodynamic limit ($Pr \to 0$ and $R \to 0$) for arbitrary inclination. In this limit the governing parameter is the Grashof number $Gr = R/Pr$, which controls the ratio between the inertial and viscous forces. The temperature disturbances are homogenized instantaneously and therefore, in regard to the perturbative flow, the buoyancy forces are absent. In the formal $Pr \to 0$ and $R \to 0$ limit, the basic profiles are $w_b(x) = \sin\alpha(x^3 - x)/6$ and $\theta_b(x) = 0$ and the equation for the amplitude of transversal perturbations is the well-known Orr-Sommerfeld equation whose solution gives $Gr_{ST} = 495/\sin\alpha$ and $k_{ST} = 1.345$. The asymptotic trends for $Pr \to 0$ of Gr_{ST} and k_{ST} are shown with dashed lines in Fig. 9(a,b) together with the values obtained from the solution of Eqs. (5)–(7) at several values of Pr and α.

It is remarked that the asymptotic limit fails for small enough inclinations and for $Pr > 0.05$ [this is clearly seen in Fig. 9(b)]. As the Prandtl number increases the thermal effects becomes increasingly important. The time needed to homogenize a temperature excess in a fluid parcel goes like $O(Pr\, h^2/\nu)$ and therefore, at larger Pr, the buoyant force acts on the differentially heated particles during a larger interval of time. An inspection in the trend for k_{ST} versus Pr in Fig. 9(b) indicates that the effect of buoyancy in the perturbative flow becomes relevant for $Pr > 0.05$ and depends on the inclination angle. At $\alpha = 90°$, the mean cross-stream stratification is stable and buoyancy acts as a restoring force. As a consequence, as Pr increases, the critical ST rolls reduce the relative amount of cross-stream flow (k_{ST} decreases) and the ST perturbation is finally damped for $Pr > 0.12$ (this fact is confirmed also by numerical calculations [16]). For $\alpha > 90°$, the fluid is also stably stratified along the z direction and as shown in Fig. 4, the ST rolls are damped at even lower values of Pr.

According to the stability analysis, for $\alpha < 90°$ the ST rolls can be observed at relatively large values of Pr (~ 1)

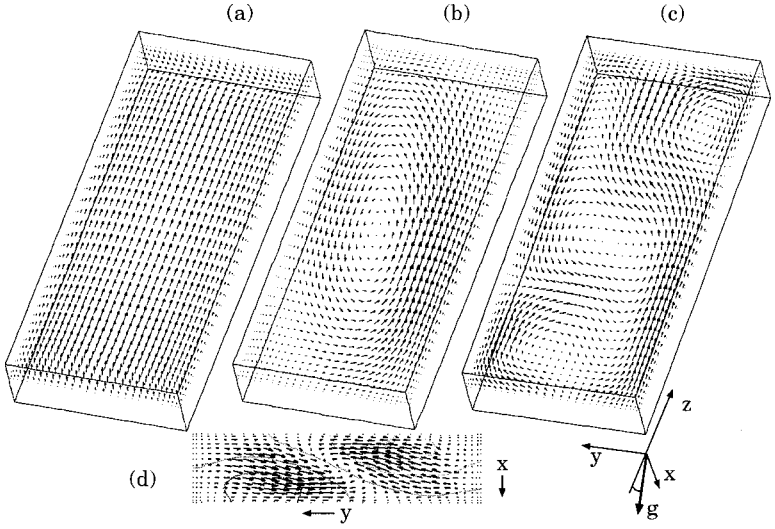

FIG. 8. Cuts of the velocity field at $x = -0.152h$ obtained for $Pr = 6.7$, $\alpha = 20°$, $A_y = 1/3$, and $A_z = 1/7$ and at: (a) $Ra = 25$ (basic unicell); (b) $Ra = 30$ (primary SL_l mode); and (c) $Ra = 35$ (the secondary mode). (d) The projection of the velocity field at $z = 0.47L$ and $Ra = 30$.

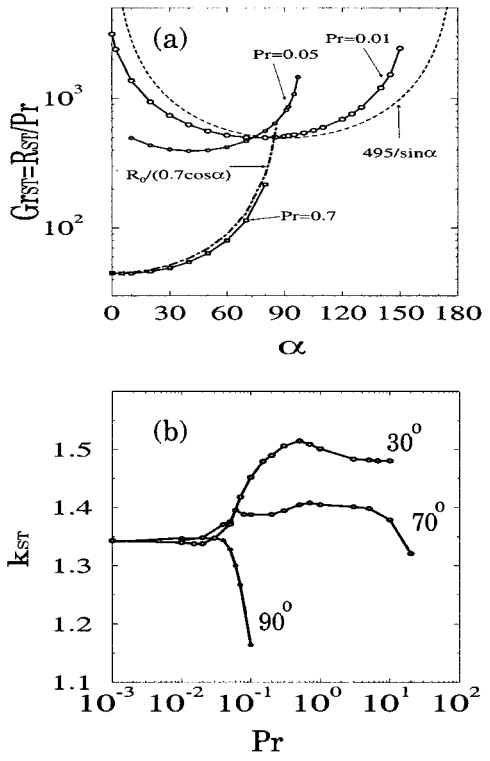

FIG. 9. (a) The critical Grashof number $\mathrm{Gr}_{ST}=R_{ST}/\mathrm{Pr}$ versus α. (b) The critical wave number k_{ST} versus Pr.

and with larger wave numbers [see Fig. 9(b)]. As discussed in Ref. [18], this is a consequence of the following thermal mechanism: owing to the mean cross-stream temperature difference, fluid particles moving along x direction carry their local temperature to a new thermal surrounding where they are accelerated by the streamwise buoyancy force, which draws within an unstable stratification. Anyhow, at $\mathrm{Pr}\to\infty$, $R_{ST}\to R_0/\cos\alpha$, which corresponds to $\mathrm{Ra}\to\infty$ (see Fig. 3). Hence, as Ra is increased, in an enclosure filled with a large enough Pr fluid, the BLR shall appear before the ST instability can develop ($R_{BLR}<R_{ST}$). In this case, the streamwise temperature gradient vanishes at the core region and the above-explained thermal mechanism is absent; as a consequence the ST rolls are damped. The frontier of this criterion is shown for different aspect ratios in the stability map of Fig. 4. Note that the destabilizing effect of the streamwise component of buoyancy is enhanced if the cavity is made larger. For instance, for $A_z=1/50$ a small inclination (of about 4°) with respect to the horizontal position is enough to enable ST rolls in gases ($\mathrm{Pr}\sim 1$).

1. Numerical calculations

Table III compares the main numerical results concerning the onset of multicellular flow in 2D cavities. In these numerical calculations, accuracies of about 1% in the flow quantities were ensured by successive mesh refinement (see Ref. [25] for details). The wave number was obtained from the maximum amplitude peak in the the Fourier spectra of the z dependence of several flow quantities. Calculations made for $\mathrm{Pr}=0.7$ confirmed the possibility of finding ST rolls in gas-filled heated-from-below inclined cavities. For $\mathrm{Pr}=0.7$, the multicellular flow developed gradually above values of Ra slightly smaller than the predicted critical ones (see Table III). These transitions are examples of imperfect bifurcations induced by recirculation eddies formed near the end walls and are quite similar to those reported by Hart [13]. Using $\mathrm{Pr}=0.7$ and $A_z=1/10$, the ST rolls were observed at inclinations up to $\alpha=70°$. At $\alpha=80°$, the Rayleigh number was increased up to $\mathrm{Ra}=2.0\times10^3$, but no trace of ST rolls was found. Instead, the unicell reached a fully developed BLR above $\mathrm{Ra}>1.3\times10^3$. This result agrees quite well with the stability criteria derived according to the onset of the BLR ($R_{crit}>R_{BLR}$), which predicts that the ST rolls cannot develop for $\alpha>75°$ (see Fig. 4). Also, for $\mathrm{Pr}=6.7$, the ST rolls did not appeared for any value of α, neither in the 2D cavity ($A_z=1/7$) nor in the 3D one ($A_z=1/7$, $A_y=2/3$).

In order to investigate the effect of the third dimension, numerical calculations were carried out in a 3D cavity with $A_z=1/10$ and $A_y=1$, using $\mathrm{Pr}=0.05$ and $\alpha=10°$. Results obtained with $15\times15\times45$ calculation cells agreed within about 6% with those obtained with $15\times15\times90$. The time step was about $10^{-3}h^2/\nu$. At $\mathrm{Ra}=50$ ($R=37.5$), the basic flow was disrupted by two stationary shear rolls. As illustrated in Fig. 10(b) the resulting bicellular flow maintains essentially a bidimensional structure. The wavelength of the transversal rolls is approximately $6H$, which gives a wave number ($k=0.52$) smaller than the prediction for $A_y\to0$

TABLE III. Comparison between numerical results and theoretical predictions at the onset of 2D multicellular flow. The frequency is in units of (h^2/ν). The theoretical critical external Rayleigh number is $\mathrm{Ra}_{crit}=R_{crit}/K$, where ''$crit$'' stands for OT_l or ST.

Configuration			Numerical results			Theoretical prediction				
Pr	α	A_z^{-1}	$\mathrm{Ra}^{(1st)}$	Wave no.	Freq.	K	Ra_{crit}	k_{crit}	f_{crit}	Instability
0.025	10°	30	(24,27]	1.31	-	0.92	26.94	1.35		ST
0.7	20°	10	>110	1.5		0.27	119.07	1.52		ST
0.7	50°	10	>160	1.5		0.25	178.72	1.47		ST
0.7	70°	10	>700	1.4		0.11	727.18	1.41		ST
0.7	20°	50	45	0.35	0.87	0.70	44.57	0.35	0.68	OT_l
0.7	50°	50	75	0.31	1.15	0.58	73.75	0.31	0.96	OT_l
0.3	12°	60	(35,38]	1.53/0.25	-/0.82	0.84	36.42	1.53	-/0.76	ST+OT_l

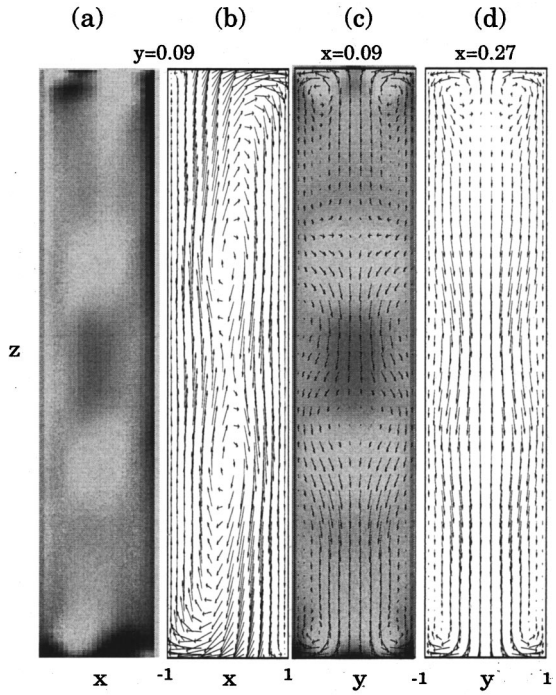

FIG. 10. Snapshots of the 3D stationary flow for Pr=0.05, $\alpha=10°$, $A_y=1$, $A_z=1/10$ at Ra=50. (a) Isovalues of the field $\nabla^2 P$ (dark regions corresponds to $\nabla^2 P<0$ and vice versa). (b) The velocity field in the same plane of (a), $y=0.09$. (c) Isovalues of $\nabla^2 P$ in the $x=0.09$ plane showing also the velocity field. (d) The velocity field in the plane $x=0.27$.

($k_{ST}=1.35$). The increase of lateral confinement implies larger momentum dissipation and therefore an increase of the critical Rayleigh number and wavelengths. In particular, our result for the 3D configuration is in concordance with the results of Nikitin *et al.* [27] who obtained a wavelength of $6H$ for a Pr=0 fluid in a horizontal $A_y=1/10$ cavity.

The 3D calculations revealed a subtle three-dimensional effect that induces flow along the y direction once the two-vortex pattern is developed. This flow, shown in Fig. 10, can be explained by considering the low pressure spots generated around the core of each vortex [at $x=0$, $y=0$, and $z\simeq\{0.67,0.32\}(L/h)$]. Figures 10(a) and 10(c) illustrate the distortion of pressure field by showing the isovalues of $\nabla^2 P$. Note that the pressure decreases inwards (towards the center of the cavity) where $\nabla^2 P>0$ (lighter regions) and outwards where $\nabla^2 P<0$ (darker regions). Near each vortex, the low pressure spots generate a suction force that impels flow along the y direction towards the center of each roll [see Fig. 10(c)]. At the inter-vortex region, conservation of mass requires outflow towards the $y=\pm 1$ walls. Moreover, at this region the two corotating rolls collide with opposite x (inwards) velocities and therefore the pressure locally increases ($\nabla^2 P<0$) producing an outward pressure force that draws flow towards $y=\pm 1$. The resulting velocity pattern in the YZ sections [shown in Figs. 10(c) and 10(d)] has a sinusoidal structure around the $x=0$ plane, which gradually recovers a Poiselle-like profile near $x=\pm 1$, i.e., away from the vortex core. Two new transitions were observed at relatively small increases of Ra (Δ Ra=5). An analysis of these transitions shall be presented elsewhere and we refer to Ref. [25] for illustrations. Briefly, at Ra=75 the two cells merge to a unique stationary roll centered at $z=0.5L/h$ (a flow essentially similar to that inferred by the experiments of Ref. [28]) and at Ra=80 an oscillatory and three-dimensional flow (composed by the centered shear roll and one perpendicular roll in the YZ plane) was developed.

The numerical results indicate that the $\alpha<90°$ configuration enables the oscillation of transversal rolls at values of Pr larger than those found for the horizontal configuration and that as α decreases, successive scenarios are separated between relatively shorter intervals of Ra. For instance, no oscillatory regimes were found in the experimental and numerical work by Braunsfurth *et al.* [28] (they used Pr $=0.015$ in a $1\times1\times4$ cavity). Still for $\alpha=90°$, Skeldon *et al.* [19] found that increasing Pr up to Pr=0.025 inhibits the onset of oscillations, but Ref. [21] reports that a Hopf bifurcation occurs for Pr=0.025 if the configuration used in [19] is tilted to $\alpha=80°$. Also, the 3D configuration presented here indicates that for $\alpha=10°$, several multicellular patterns and oscillatory flow can be observed at least until Pr=0.05. For $\alpha<90°$ the cutoff for the oscillation of transversal rolls is shifted towards larger values of Pr, surely as a consequence of the above-mentioned destabilizing coupling between the z component of buoyancy and the cross-stream advection. Anyhow a study of the inclination effect on the Hopf-bifurcation branches at low and moderate Pr number is beyond the scope of this paper and it is left for future work.

VI. THE OSCILLATORY TRANSVERSAL LONG-WAVELENGTH INSTABILITY (OT_L)

A detailed description of the OT_l instability including the energetics of critical perturbations can be found in Refs. [18,25]). Here, we shall briefly discuss the origin of the OT_l instability and present further results on the nature of the oscillations. Numerical calculations, showing the flow produced by OT_l instability in several 2D configurations shall be also presented.

The OT_l instability is a standing wave with a rather long wavelength (typically $9H$) and it only comes up if the cavity is inclined and heated from below ($0°<\alpha<90°$). The perturbation gains the most part of its kinetic energy from the streamwise buoyant force. For $\alpha\to 0°$, the OT_l critical perturbation recovers the critical transversal mode in the vertical cavity: $R_{OT_l}\to R_0$, $k_{OT_l}\to 0$, and $f_{OT_l}\to 0$. The value of R_{OT_l} is slightly smaller than $R_0/\cos\alpha$ and does not greatly depend on Pr [18]. The critical wave number reaches its maximum value ($k_{ST}=0.36$) at $\alpha\simeq 20°$ and Pr$\simeq$1 and decreases to zero for $\alpha=90°$ or Pr$\to\{0,\infty\}$. The cross-stream motion takes energy out from the mean shear stress and also from the coupling between the cross-stream advection and the streamwise buoyancy force. This latter mechanism is essentially the same as that explained for the ST instability at Pr ~ 1

In relation to the origin of the oscillation, it can be proven (see Ref. [10]) that in the case of an odd basic profile, the oscillatory perturbations are standing waves composed by the superposition of a couple of traveling modes with equal

and opposite sign phase velocities. In the case of the OT_l instability the ratio between the phase velocity and the maximum value of the basic velocity $c_{OT_l} \equiv 2\pi f_{OT_l} k_{OT_l}^{-1} / w_{b,\max}$, only depends on the fluid diffusivities (i.e., on Pr) and does not vary with the inclination. Its value is less than 1 and fits to $c_{OT_l} = 0.91(1 - 0.08\,\mathrm{Pr}^{-1})$ for $\mathrm{Pr} > 0.1$. This fact indicates that the oscillation is essentially driven by the mean flow drag, which carries the pair of traveling modes in opposite senses of the z direction.

1. Numerical results

The OT_l cells has been observed in numerical calculations carried out at several inclinations (details can be found in [29]). As seen in Table III, the stability analysis correctly predicts the Rayleigh number and the wave number at the onset of the OT_l wave. Nevertheless, if the onset of the instability occurred well inside the transition regime, the frequency of the oscillation greatly differed from the stability analysis prediction (in worst cases about a 30% difference, see Table III). In order to understand why the confinement has a significant influence only on the frequency, the ratio between the phase velocity and the maximum mean flow streamwise velocity obtained from the numerical output c was compared with the stability prediction c_{OT_l}. In all cases, both values agreed at the onset of the multicellular flow. Therefore, the relevant parameter for the oscillation is the ratio c, and one can forecast the oscillation frequency in a closed geometry by $f_{OT_l} = c_{OT_l}(\mathrm{Pr}) w_{b,\max}$, where $w_{b,\max}$ was given in Ref. [8] in terms of Ra, α, and A_z.

In order to investigate the interaction between the ST and OT_l instabilities calculations were carried out for $\mathrm{Pr} = 0.3$ and $\alpha = 12°$; a point placed at the codimension-2 line for the ST-OT_l instabilities (see Fig. 4). The oscillatory flow appeared at $35 < \mathrm{Ra} \leqslant 38$ (see Table II) and it is illustrated in Fig. 11 showing several snapshots along a cycle. A fine mesh with 31×261 collocation points has to be used to capture the details of this multicellular flow and ensure accuracies of about 2%. As shown in Fig. 11(b), the wave number spectra of the stream function presents two peaks at values of k that coincide exactly with the prediction for ST and OT_l cells: $k_{ST} = 1.53$ and $k_{OT_l} = 0.25$. At the onset of multicellular flow the center of each shear roll remains fixed in space and the oscillation is governed by the OTl wave with $c = 0.69$. At a slightly larger value of Ra, the position of the shear rolls begins also to oscillate leading to successive transitions to quasiperiodic flow and finally to a chaotic time signal for $\mathrm{Ra} \geqslant 42$. Details on these transitions are given in Ref. [25].

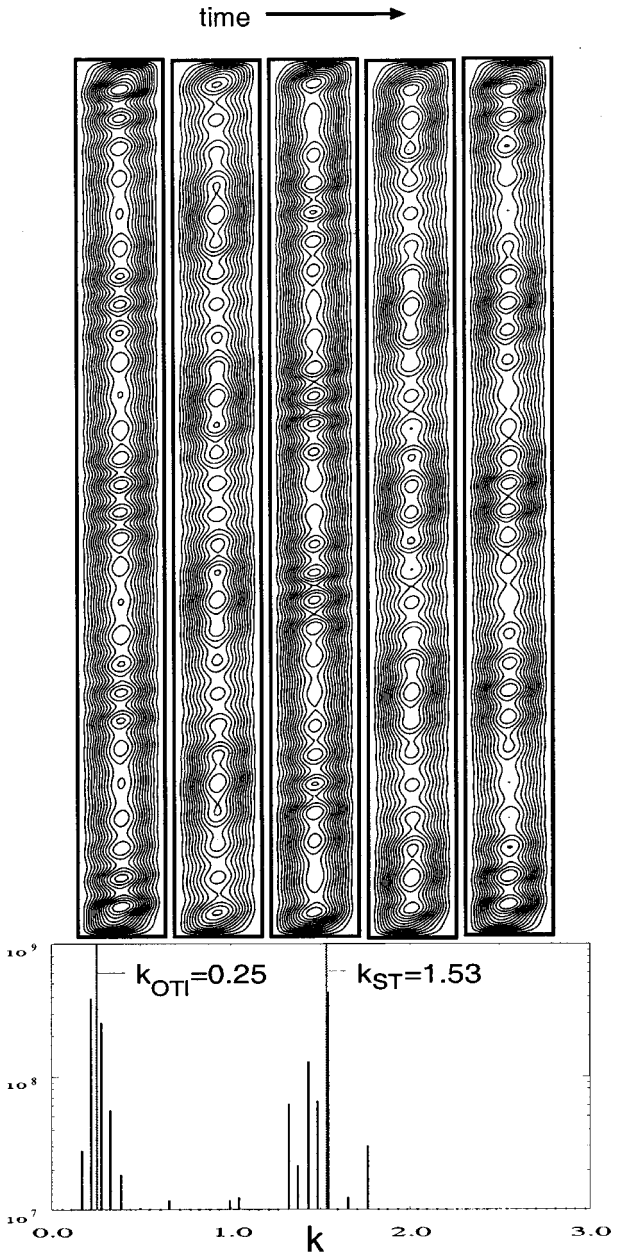

FIG. 11. Above: snapshots of the stream function along a cycle of oscillation ($f = 0.823\nu/h^2$) observed for $\mathrm{Pr} = 0.3$, $\alpha = 12°$, $A_z = 1/60$, and $\mathrm{Ra} = 38$. Below: wave number spectra along the z direction (the dashed lines indicate the critical wave numbers predicted by the stability analysis).

VII. THE STATIONARY LONGITUDINAL SHORT-WAVELENGTH INSTABILITY (SL_S)

As seen in the stability diagram of Fig. 4, the SL_s instability only takes place if the inclination is near or equal to $\alpha = 90°$. The SL_s instability was predicted in previous linear stability analysis made for the horizontal configuration [15], but it has not been explicitly reported in numerical calculations or experiments. In what follows we present the trends of the critical parameters, explain the physical origin of the instability, and finally give a further requirement for the onset of the SL_s instability, which depends on the aspect ratio of the cavity.

Table I gives a fit to R_{SL_s} and m_{SL_s}, for $\alpha = 90°$ within about 3% of error. For $\mathrm{Pr} < 0.1$, the critical Rayleigh fits to $R_{SL_s} \simeq 1700\,\mathrm{Pr}^{1/2}$ and $m_{SL_s} \simeq 2.9$. For $\alpha \leqslant 90°$, the flow becomes stable to SL_s perturbations at $\mathrm{Pr} \simeq 1$, while for $\alpha > 90°$, the stabilization occurs at much lower values of Pr (for instance, if $\alpha = 93°$ for $\mathrm{Pr} > 0.1$).

Figure 12 illustrates the perturbative SL_l flow by showing

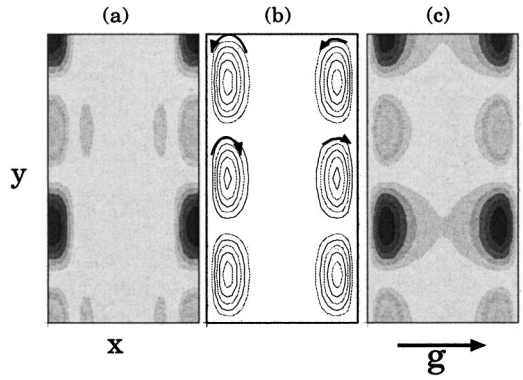

FIG. 12. (a) Isocontours of the perturbative temperature T_p, (b) stream function Φ_p, and (c) axial velocity w_p of the critical SL_s disturbance for Pr=0.3, $\alpha=90°$. In (a) and (c), darker regions correspond, respectively, to $T_p>0$ and $w_p>0$. The critical wave number is $m_{SL_s}=2.33$.

the critical mode for Pr=0.3 and $\alpha=90°$. The wavelength is approximately the semiwidth $h=H/2$, but the perturbation is localized at layers near the $x=\pm 1$ walls whose thickness is about $0.25H$. The SL_s instability is generated by a mechanism that couples the mean shear stress and the streamwise temperature gradient and takes place at unstable layers, where $w_b'>0$. The perturbative momentum along the z direction is driven by a shear force triggered by the cross-stream perturbative flow $[-R\,\mathrm{Pr}^{-1}u_p w_b']$, see Eq. (8)]. Note that at the unstable layers, $u_p w_p<0$ [see Figs. 12(b) and 12(c)] and hence the Reynolds energy $(-R\,\mathrm{Pr}^{-1}\langle u_p w_p w_b'\rangle)$ is positive. Owing to the mean streamwise temperature gradient, the perturbative advection in the z direction generates a temperature pattern in the XY plane [see Fig. 12(a)] that activates lift forces along the cross-stream direction and a perturbative flow in the XY plane, which in turn feeds the shear force. For Pr>1, the SL_s instability is damped because of the effect of the cross-stream stable stratification and the decrease of the inertial forces.

The above-described mechanism makes possible, in principle, the onset of SL_s rolls in the transition regime (TR) of a flow within a completely stable cross-stream stratification (i.e., with adiabatic walls). Nevertheless, consideration of the finite size of the cavity leads to the conclusion that for a broad range of values of the aspect ratio A_z, the boundary layer regime appears before the onset of the SL_s instability ($R_{BLR}<R_{SL_s}$). To show this fact, let us consider a favorable case: a horizontal configuration filled with a gas with Pr =0.7 (for which the OL or ST rolls cannot develop). In this case ($R_{SL_s}\simeq 10^4$ and $R_{BLR}\simeq 62.5A_z^{-1}$) the requirement $R_{SL_s}<R_{BLR}$ is only fulfilled in cavities with at least $A_z<10^{-2}$ ($L>10^2H$). In smaller cavities the SL_s instability is unlikely to be observed in the TR, although once the boundary layer regime is developed, short-wavelength longitudinal rolls may appear at the intrusion layers near the $x=\pm 1$ walls where $\partial w/\partial x$ is rather large and a negative value of $\partial T/\partial z$ is maintained by the streamwise advection [8]. Schopf and Stiller [17] have experimentally found a set of longitudinal stationary rolls of wavelength $\sim 0.125h$ arising at the intrusion layer of a $1\times 2.08\times 1$ cavity filled with water. These authors showed that, for this value of Pr(~ 7), the perturbation is mainly driven by a Rayleigh-Bénard-like mechanism arising at the unstably stratified layer formed inside the intrusive layer although they indicate that shear effects may have a certain destabilizing contribution. This contribution comes out from the above-mentioned $(\partial T/\partial z]$-$[\partial w/\partial x)$ coupling and a possible way to experimentally measure its relative importance is to find the trace of the sinusoidal pattern of the perturbative streamwise velocity in the XY plane [see Fig. 12(c)], which would be completely absent if the longitudinal rolls were uniquely driven by a Rayleigh-Bénard-like instability [25].

VIII. THE OSCILLATORY LONGITUDINAL INSTABILITY (OL)

The OL instability arises at low enough Pr number and typically for $\alpha<115°$ (see Fig. 4). Table I shows the trend of the critical parameters with Pr, fitted within about 3% of deviation to the stability results obtained at $\alpha=90°$ and Fig. 13 plots the values of R_{OL}, m_{OL}, and f_{OL} against α for different values of Pr. The OL instability is damped at a certain cutoff value of Pr, which decreases with the inclination angle. For example, for $\alpha=90°$ and 80°, OL perturbations are damped for $\mathrm{Pr}\geqslant 0.21$ and $\mathrm{Pr}\geqslant 0.26$, respectively.

The basic mechanism that originates the OL instability can be explained by considering the limit $\mathrm{Pr}\to 0$ with finite R ($\mathrm{Gr}\to\infty$). In this limit, $\nu\to 0$, $\kappa\to\infty$ and the characteristic mean diffusion time is $h^2/(\nu\kappa)^{1/2}$. Gill [12] considered the formal equations at this $\mathrm{Pr}\to 0$ limit concluding that dissipation of momenta vanishes ($\boldsymbol{\nabla}^2\mathbf{v}\to 0$) and therefore the oscillatory flow arises as a consequence of a dynamical balance between the inertial and buoyant forces. Also, the advection of heat is balanced instantaneously with the thermal diffusion, $\partial T/\partial t\to 0$. Hart [13] proposed another set of equations for $\mathrm{Pr}\to 0$. The momentum equation agreed with that derived by Gill, but the energy equation was treated in a different way. Hart assumed that heat is transfered without any loss of energy by conduction and hence that the perturbation behaves like a pure thermal wave (i.e., $dT/dt=0$). Although a number of numerical and experimental works have investigated the OL wave (see e.g., [20,22] and references therein), any explanation on the discrepancies of both theoretical models could be found in the literature.

In what follows, an analytical approach inspired in the approximation done by Gill [12] is presented. It intends to give an insight into the effect of inclination on the OL instability and also provides a criteria for the validity of Gill's and Hart's approaches. Following Gill [12], we consider the following simplification of the disturbance, which mimics the perturbative flow around the central part of the layer ($x\sim 0$):

$$w_p(x,y,z)\simeq\cos(d_M x)\cos(my)\tilde{w}_p(t),$$

$$\Phi_p(x,y,z)\simeq\cos(d_M x)\sin(my)\tilde{u}_p(t),$$

$$T_p(x,y,z)\simeq\cos(d_T x)\cos(my)\tilde{T}_p(t). \qquad (12)$$

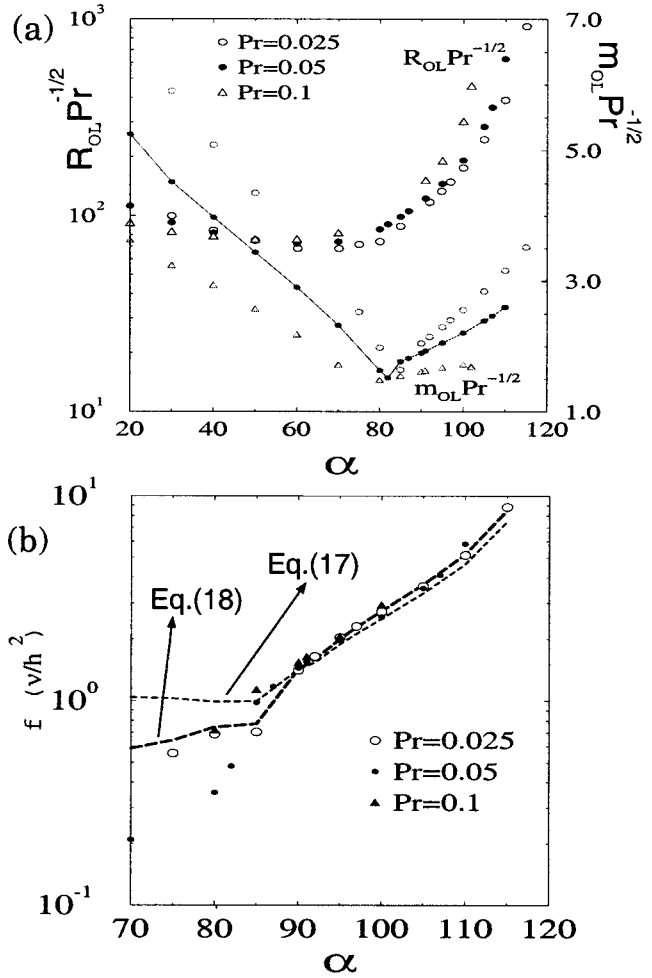

FIG. 13. (a) The critical Rayleigh number (left axis) and wave number (right axis) of the OL instability, both scaled with $Pr^{1/2}$. (b) The critical frequency f_{OL} against α [points correspond to the stability results and dashed lines correspond to Eqs. (17) and (18) evaluated with the critical parameters obtained for Pr=0.025]. Both theoretical trends have been divided by a factor of 2.2.

In Eqs. (12) we have introduced scalars representing the effective temperature and momentum diffusion along the x direction, d_T and d_M. Gill [12] used $d_M=\pi/2$, which guarantees the Dirichlet boundary condition at $x=\pm 1$ for w_p and $u_p=\partial\Phi_p/\partial y$ but not for $v_p=-\partial\Phi_p/\partial x\neq 0$. Nevertheless, the simplified flow given by Eq. (12) is useful enough to draw the main characteristics of the perturbation around $x\sim 0$, away from the thin Stokes layers near the walls whose thickness $[O(Pr^{1/2})]$ vanishes as $Pr\rightarrow 0$. Gill [12] also used $d_T=\pi/2$, which adequately represents the perturbative temperature field inside perfectly conducting walls (i.e., Dirichlet thermal boundary conditions). As shown below, a coherent choice of the value of d_T depends on the type of walls. From Eq. (12), the Laplacian operator simplifies to a scalar given by $n_M^2=m^2+d_M^2$ for momentum related quantities and $n_T^2=m^2+d_T^2$ for the temperature.

Consider a positive disturbance of velocity along the z axis, $\tilde{w}_p(t_0)>0$, made at an instant t_0 around the center of the layer ($x=0$, $y=0$). The perturbative flow at a time $t=\delta t$ shall be described by expanding the equations for the longitudinal disturbances [Eqs. (8)–(10)] to first order in time. This leads to

$$\mathrm{Pr}^{1/2}\tilde{T}_p+n_T^2\tilde{T}_p\delta t=\tilde{w}_p(t_0)\,\delta t, \tag{13}$$

$$n_M^2\tilde{u}_p=-m^2R\,\mathrm{Pr}^{1/2}\sin\alpha\tilde{T}_p\delta t, \tag{14}$$

$$\tilde{w}_p=\tilde{w}_p(t_0)+\tilde{u}_p|\hat{w}_b'|R\,\mathrm{Pr}^{-1/2}\delta t. \tag{15}$$

It is remarked that in Eqs. (13)–(15) and in what follows, the following scales for velocity, temperature, and time shall be used: $R\kappa/h$, $Rh(\Delta T/L)$, and $h/(\nu\kappa)^{1/2}$.

In Eq. (15) the mean shear has been substituted by an averaged value that gives a larger weight in the central part of the layer (e.g., $\widehat{w_b'}\equiv\int_0^1 w_b(x)'\cos^2(\pi x/2)dx$). Note that around $x=0$, the mean shear is negative and $\widehat{w_b'}=-|\widehat{w_b'}|$. In Eq. (13) the heat advected along the x direction has been neglected. As discussed by both Gill [12] and Hart [13], this term is negligible at low Pr (its contribution goes like $Pr^{1/2}$) and at larger Pr it has a stabilizing effect. The basic mechanism of the oscillation is deduced from Eqs. (13)–(15). Consider an initial velocity disturbance in the z direction with $w_p(t_0)>0$. The disturbance carries heat and locally increases the temperature [$\tilde{T}_p>0$ in Eq. (13)]. As a consequence lift forces are activated along x direction: fluid particles ascend [$\tilde{u}_p<0$ in Eq. (14)] and counter-rotating rolls are created by continuity in the XY plane. The flow along the x direction induces a shear force along the z direction that has a sign opposite to $\tilde{w}_p(t_0)$ [see Eq. (15)]. At a quarter of cycle, $\tilde{w}_p$ changes sign driven by the shear force and so does the streamwise advection, leading to $\tilde{T}_p<0$. At this point, the buoyant force acts against the ascending x flow and finally changes its sense ($\tilde{u}_p>0$). The same process takes place along the other half of the cycle but with all the perturbative quantities having a changed sign. In particular, for the initial condition proposed above, the change of sign of $\tilde{w}_p$ occurs at a quarter of a cycle so to obtain an estimation for the frequency one can let $\tilde{w}_p=0$ at $\delta t=f^{-1}/4$ in Eqs. (13)–(15). After some algebra this leads to

$$n_T^2f^2+4\,\mathrm{Pr}^{1/2}f^3=\frac{R^2m^2\sin\alpha|w_b'|}{4^2n_M^2}. \tag{16}$$

The trend for f depends on the relative importance of the two terms of the left-hand side of Eq. (16). The term $n_T^2f^2$ comes out from the the thermal diffusion and $4\,\mathrm{Pr}^{1/2}f^3$ from the explicit time derivative of the temperature. Their ratio is $f\tau_d$, where, in units of $h^2/(\nu\kappa)^{1/2}$, $\tau_d\equiv 4\,\mathrm{Pr}^{1/2}/n_T^2$ is approximately the time needed by diffusion to homogenize the temperature fluctuation along one wavelength ($\pi h^2/n_T^2\kappa$). Two different situations arise. If $f>n_T^2/4\,\mathrm{Pr}^{1/2}$, the characteristic diffusion time is long compared to the period of the oscillation and the amount of energy diffused along each cycle can be neglected. In the opposite case, $f<n_T^2/4\,\mathrm{Pr}^{1/2}$, thermal diffusion balances almost instantaneously with advection in

such a way that the temperature perturbation is slaved to the perturbative axial velocity ($\nabla^2 T_p = w_p$). In view of Eq. (16), one should expect that this former condition stands for Pr $\to 0$ as stated by Gill [12]. But in the case of adiabatic walls at low Pr, the isothermals of the critical disturbances are nearly parallel to the x direction[2] leaving a vanishingly small thermal diffusion along the x direction [i.e., $d_T \simeq 0$ in Eq. (12) and $n_T^2 \simeq m^2$]. Under this situation we have verified that, even for Pr$\to 0$, the inequality $f_{OL} > m_{OL}^2/4\,\mathrm{Pr}^{1/2}$ holds for the whole range of α and hence the term proportional to f^2 can be neglected from Eq. (16). This leads to the following trend that coincides with that proposed by Hart [13] for $\alpha = 90°$,

$$f \simeq \frac{1}{4}\left(\frac{R^2 m^2 \sin\alpha\,\mathrm{Pr}^{-1/2}|w_b'|}{n_M^2}\right)^{1/3}. \tag{17}$$

It is remarked that Eq. (17) does not take into account the effect of the streamwise component of the buoyant force. In order to include it in the theoretical model of Eqs. (13)–(15), the term $\mathrm{Pr}^{1/2} R \cos\alpha \tilde{T}_p$, has to be added to Eq. (15). This leads to

$$f \simeq \frac{1}{4}\left(\frac{R^2 m^2 \sin\alpha\,\mathrm{Pr}^{-1/2}|w_b'|}{n_M^2} - 4fR\cos\alpha\right)^{1/3}. \tag{18}$$

The relations of Eqs. (17) and (18) can be used to analyze the dependence of critical frequency on α. Figure 13(b) shows the values of f_{OL} against α for several Pr. The dashed lines in Fig. 13(b) are obtained by inserting the values of the critical parameters for Pr$=0.025$ into Eqs. (17) and (18) and then dividing by a factor of 2.2. As shown in Fig. 13(b) for $\alpha \geqslant 90°$, the increment f_{OL} with α agrees quite well with the trend proposed in Eq. (17). Even for the largest angle ($\alpha = 115°$), the correction of Eq. (18) is smaller than 10% and thus f_{OL} can be adequately described by Eq. (17). In view of Eq. (18), this means that the critical frequency is much larger than $(R\cos\alpha)^{1/2}/4$, which [in units of $(\nu\kappa)^{1/2}/h^2$] corresponds to the Brunt Vaisala cutoff frequency for excitation of internal gravity waves in a the cavity with stable vertical stratification.

On the contrary, for $\alpha < 90°$ the streamwise buoyant has a relevant effect in the critical period. As shown in Fig. 13(b), for α below 90° the value of f_{OL} decreases faster than predicted by Eq. (17) and fits much better to the trend given by Eq. (18). Note that if the cavity is heated from below the streamwise buoyant force amplifies the perturbative flow along the z direction if $w_p T_p > 0$. This occurs along almost the whole cycle because at low Pr, w_p and T_p oscillate practically in phase (see [12]). Hence, in that part of the cycle when the mean shear tends to change the sign of w_p (acting as a restoring force) the axial buoyant force pulls in the opposite sense and as a consequence, the period of oscillation increases. Owing to this mechanism, at low enough values of

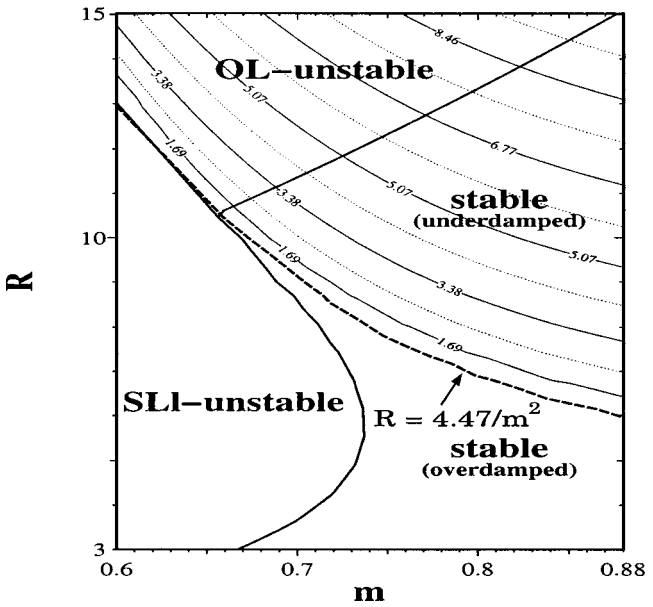

FIG. 14. Neutral curve and isovalues of the imaginary part of the growth rate λ_i for Pr$=0.02$ and $\alpha = 50°$. The dashed line at $Rm^2 = 4.47$ indicates the exchage of stability from $\lambda_i = 0$ to $\lambda_i \neq 0$.

R or m, the streamwise buoyancy is able to damp the oscillatory modes. This fact can be seen in Fig. 14 where the isovalues of the imaginary part of the complex growth rate λ_i, are drawn in the R-m chart. According to Eq. (18) the oscillatory perturbations disappear for $Rm^2 \sim f\,\mathrm{Pr}^{1/2}\cot\alpha/|w_b'|$, a trend that qualitatively agrees with the results of the linear stability analysis.

1. Numerical calculations

Numerical simulations for a Pr$=0.025$ fluid (mercury) were carried out in a 3D cavity with $A_z = 1/4$, $A_y = 1/6$, and $\alpha = 80°$. The numerical details and a discussion of the nonlinear evolution of this flow can be found in Ref. [21]. Accuracies of about 5% were guaranteed by comparing the results of the oscillatory flow obtained with $15\times46\times35$, $15\times46\times71$, and $15\times91\times35$ calculation cells and using time steps about 100 smaller than the fundamental period.

The basic unicellular flow breaks down owing to a ST shear roll that for Ra>15 gradually develops at the center part of the cavity according to an imperfect bifurcation induced by the confinement. The flow remains bidimensional and stationary until an oscillatory 3D instability develops at $40 < \mathrm{Ra} \leqslant 47$. The resulting flow is composed by three longitudinal (counter-rotating) rolls along the y direction and it is illustrated in Fig. 15 for a slightly greater value of Ra. At Ra$=47$ the local Rayleigh number at the core is $R = K\,\mathrm{Ra} = 40$, the wavelength is approximately $4H$ ($m = 0.785$) and the frequency is $f_{num} = 3.27\nu/h^2$. According to the linear stability analysis, the frequency of the OL disturbance at these values of R and m is $f_0 = 3.45\nu/h^2$, very close to the outcome of the numerical calculation.

As Ra is increased, the fundamental frequency of the flow obtained from the numerical calculations fits to $f_{num} = 0.10\,\mathrm{Ra}^{3/7}(\nu\kappa)^{1/2}/h^2$ within less than 2% of error. Let us compare this trend with the theoretical predictions in Eqs.

[2]Note that this is not possible in the conducting case considered by Gill [12].

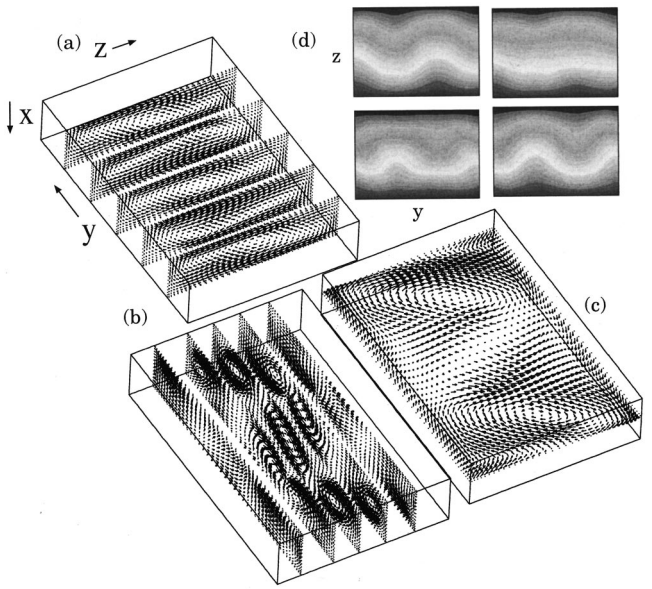

FIG. 15. Snapshots of the flow induced by the OL instability in a cavity with $A_y=1/6$, $A_z=1/4$, $\mathrm{Pr}=0.025$, $\alpha=80°$, and $\mathrm{Ra}=62$. (a), (b), and (c) show cuts of the vector field at, respectively, $y=cte$, $z=cte$, and $x=0$ planes. In (d), four snapshots of the isothermals at $x=0$ along a semiperiod of the cycle [time increases from left to right and from top to bottom; the upper left isothermal field corresponds to the same instant of (a), (b), and (c)].

(17) and (18). First, in order to evaluate $R=K\,\mathrm{Ra}$, we have measured K by averaging the temperature gradient at the core (between $L/4<z<3L/4$) along one oscillation cycle. As shown in [21], the result fits to $K=2.6\,\mathrm{Ra}^{-2/7}$ within about 5% of error. The maximum value of the mean streamwise velocity increases like $w_{b,\max}=0.31\,\mathrm{Ra}^{4/7}\kappa/h$ [8] and it is located near $|x|=1/2$, hence $|\hat{w}_b'|\simeq 2w_{b,\max}$. Introducing these trends for K and $|\hat{w}_b'|$ and $m=0.785$ into Eq. (18), one obtains that at $\mathrm{Ra}=47$, the term proportional to $\cos\alpha$ is less than 0.03 times the term proportional to $\sin\alpha$. Moreover, both terms increase, respectively, like $\mathrm{Ra}^{9/7}$ and $\mathrm{Ra}^{8/7}$, so the correction associated with the streamwise component of buoyancy can be neglected. The trend resulting from Eq. (17) yields $f=0.28\,\mathrm{Ra}^{3/7}(\nu\kappa)^{1/2}/h^2$, which fits to the power law observed in the numerical calculations, $f_{num}=0.10\,\mathrm{Ra}^{3/7}(\nu\kappa)^{1/2}/h^2$. Remark that the theoretical approximation (17) overestimates f_{num} and f_{OL} [see Fig. 13(b)] in relatively close factors, respectively, 2.8 and 2.2.

It is interesting enough that for $\alpha=80°$, the correction proportional to $R\cos\alpha$ in Eq. (18), is significant for the values of the critical parameters ($m_{OL}=0.3$ and $R_{OL}=13$) but results negligible in the confined configuration (for which the instability was observed at $m=0.78$ and $R>40$). This means that the slowing down of the OL oscillations due to the effect of the streamwise buoyant force can be only observed in wide enough cavities [$A_y\geqslant O(10)$], which enable the development of the critical mode with a rather long wavelength. This phenomenon could be relatively easy to observe in an experimental set up although it demands a relatively large computational effort for a numerical investigation in view of the large depths required.

IX. CONCLUSIONS

This investigation concerns the primary flow instabilities arising on the core of rectangular inclined boxes with an imposed end-to-end temperature difference (see Fig. 1). Consideration is made of the whole range of the Prandtl number $0\leqslant\mathrm{Pr}\leqslant\infty$ and inclinations $0°\leqslant\alpha\leqslant180°$. The linear stability analysis of the basic plane-parallel flow predicts a set of instabilities whose properties are summarized in Table I. The stability diagram of Fig. 4 shows the most dangerous kind of disturbance at each point of the Pr-α space. The onset of instabilities at the core region of the cavity depends on a flow-dependent parameter (the local core Rayleigh number, $R\equiv K\,\mathrm{Ra}$) that has been calculated as a function of Ra, α and the cavity size by means of an analytical model for the confined mean flow. This calculation not only permits to state the stability results in terms of flow-independent parameters, but gives further relevant information concerning the $\alpha<90°$ case. For this range of inclinations and regardless of the cavity size, as $\mathrm{Ra}\to\infty$, R tends asymptotically to a constant value, $R_0/\cos\alpha$ ($R_0=31.285$). Also, above a calculated value of R ($R>R_{BLR}\simeq R_0/\cos\alpha$) the steady unicell changes gradually to a boundary layer regime in which the core region remains stable to any type of perturbation. By comparing the critical R for each instability with R_{BLR} we have obtained a stability criteria, which not only depends on Pr and α but also on the aspect ratio A_z. The resulting frontier of stability has been validated by numerical calculations.

In a tilted configuration with $\alpha<90°$, the fluid is stably stratified along the cross-stream direction whereas unstably stratified in the perpendicular (streamwise) direction. This fact enables either stabilizing or destabilizing couplings between the perturbative momentum and temperature, which are not possible in the vertical or horizontal limit. In particular, for $\alpha<90°$ and $\mathrm{Pr}\geqslant O(1)$, transversal perturbations take kinetic energy out from the buoyant excess generated by the cross-stream perturbative advection. As a consequence the ST rolls become unstable even in gases ($\mathrm{Pr}\sim1$). Also, for $0°<\alpha<90°$ and moderate Pr, an oscillatory transversal instability (OT_l) is observed with a wavelength of about ten times the width of the cavity and with a phase velocity proportional to the mean flow drag. On the contrary, tilting the cavity towards $\alpha<90°$ has a stabilizing effect on the long wavelength stationary thermal mode, which arises in the unstably stratified vertical cavity ($\alpha=0°$). In the inclined configuration these type of perturbations are damped for wave numbers larger that a predicted cutoff value (m_{CUT}). An important consequence of this fact is that in inclined long cavities the Rayleigh-Bénard instability can be avoided by using $A_y>m_{CUT}/\pi$, as confirmed by numerical calculations in 3D geometries.

In relation to the oscillatory longitudinal (OL) instability, we have derived an analytical approach that yields a criterion for the applicability of the previous theoretical trends proposed for the OL frequency [13,12]. In particular the trend proposed by Hart [13] is applicable when the period of the OL wave is smaller than the characteristic thermal diffusion time along a wavelength: a situation that arises in the case of adiabatic walls. The theoretical model also gives insight into

the effect of inclination. For $\alpha > 90°$, the streamwise buoyant force has no direct influence on the critical frequency, which grows like $(R_{OL}^2 \sin\alpha)^{1/3}$. The reason for this fact is that the critical frequency is much larger than the Brunt-Vaisala cutoff frequency for excitation of internal gravity waves. On the contrary, for $\alpha < 90°$ the streamwise buoyant force tends to reduce the critical frequency as α decreases. Anyhow, its relative contribution to the frequency goes like $\mathrm{Pr}^{1/2}\cot\alpha/Rm^2$ and turns out negligible in the cavity considered for numerical calculations ($A_z = 1/4$, $A_y = 1/6$, $\alpha = 80°$, and $\mathrm{Pr} = 0.025$) because of the large values of m and R at which the OL instability appears.

As a final conclusion, the inclined configuration introduces a new dimension in the space of parameters and permits access to several lines of codimension-2 by a suitable choice of the operating parameters. As proved by previous experiments and numerical calculations of this type of flow [22–24,21], a rich dynamical behavior arises around these lines as a consequence of the competition between several type of instabilities. By indicating the locus of the primary instabilities in the space of parameters (Pr, α, and aspect ratios), one of the motivations of this work is to provide the necessary information for this kind of investigations in an alternative experimental setup that may be simpler than those currently used in the literature [22,24].

ACKNOWLEDGMENTS

The author acknowledges discussions with E. Crespo del Arco, I. Zuñiga, J. García Sanz, P. Bontoux, and useful comments of Professor De Vahl Davis and Professor Gershuni. This work has been supported by DGICYT Projects Nos. PB96-0148 and PB98-0074 and A.I. HF1998-0079. Part of the calculations in 2D have been carried out on Cray YMP2E and CRAY C98 computers with support from IMT in Chateau-Gombert, Marseille. The 3D computations were carried by a commercial code and local computer resources (STORM, Pacific Sierra Corp.).

APPENDIX: GOVERNING EQUATIONS AND NUMERICAL METHODS

The nondimensional continuity, Navier-Stokes and energy equations have been obtained by using h, h^2/ν, $g\beta\Delta T h^3/L\nu$, ΔT, and $\rho_o g\beta\Delta T h^2/L$ as scales of length, time, velocity, temperature, and pressure,

$$\nabla\cdot\mathbf{v} = 0, \tag{A1}$$

$$\frac{\partial\mathbf{v}}{\partial t} + \mathrm{Gr}\mathbf{v}\cdot\nabla\mathbf{v} = -\nabla P + \nabla^2\mathbf{v} - 2A_z^{-1}T\mathbf{e}_g, \tag{A2}$$

$$\mathrm{Pr}\frac{\partial T}{\partial t} + \mathrm{Ra}\,\mathbf{v}\cdot\nabla T = \nabla^2 T. \tag{A3}$$

The boundary conditions corresponds to adiabatic rigid walls (no-slip condition assumed)

$$\mathbf{v} = 0 \quad \text{at} \quad x = \pm 1, \quad y = \pm A_y^{-1}, \quad z = \{0, 2A_z^{-1}\}, \tag{A4}$$

$$T = 0 \quad \text{at} \quad z = 0, \quad T = -1 \quad \text{at} \quad z = 2A_z^{-1}, \tag{A5}$$

$$\nabla T\cdot\hat{\mathbf{n}} = 0 \quad \text{at} \quad x = \pm 1 \quad \text{and} \quad y = \pm A_y^{-1} \tag{A6}$$

where $\hat{\mathbf{n}}$ is the surface unitary vector at the lateral walls.

The 2D flow in the XZ plane can be described by the equation for the y component of the vorticity ω_y and the heat equation, Eqs. (1) and (2). A stream function Ψ can be defined in such a way that $\nabla^2\Psi = \omega_y$, and at the walls $\Psi = \nabla\Psi\cdot\hat{\mathbf{n}} = 0$. The resulting equations written in vorticity-stream function variables have been solved by means of a Chebyshev-collocation method. The code was developed according to the detailed explanation given in previous works (see Ref. [30]). The spatial approximation in both directions is done by expanding the flow variables in a truncated series of Chebyshev polynomials and the time discretization is obtained through an Adam-Bashforth, second order Backward Euler scheme. The equations for the stream function and vorticity consist of a Stokes-type problem, which is solved by using the Influence Matrix technique [30].

In order to obtain the 3D flow, the Eqs. (A1)–(A6) have been solved by means of a commercial code[3] based on the finite volume method. The time discretization was done by means of a second order forward scheme and the spatial accuracies were of second order. The code uses the PISO algorithm [31] to couple the pressure and the velocity fields. Details of the meshes, time step, and accuracies were given in the text for every specific 2D and 3D calculations.

[3]CFD2000, Adaptive Research, Pacific Sierra Corp., 1997.

[1] A. Bachran, P. Reinshaus, and W. Seifert, Cryst. Res. Technol. **33**, 1 (1998).
[2] B. L. Markham and F. Rosenberger, J. Cryst. Growth **67**, 241 (1984).
[3] G. S. H. Lock and J. Fu, J. Heat Transfer **115**, 167 (1993).
[4] A. W. Woods and S. J. Lintz, J. Fluid Mech. **241**, 59 (1992).
[5] D. E. Cormack, L. G. Leal, and J. Imberger, J. Fluid Mech. **65**, 209 (1974).
[6] B. Boehrer, Int. J. Heat Mass Transf. **40**, 17 (1997).
[7] R. A. Wirtz and W. F. Tsheng, in *Natural Convection in Enclosures*, edited by J. Catton and K. E. Torrance (ASME, New York, 1980), Vol. 8, pp. 67–54; *Numerical Methods in Thermal Problems I*, edited by Lewis and Morgan (Pineridge Press, UK, 1979), pp. 381–390.
[8] R. Delgado-Buscalioni and E. Crespo del Arco, Int. J. Heat Mass Transf. **44**, 10 (2001); **44**, 1947 (2001).
[9] T. Adachi and J. Mizushima, J. Phys. Soc. Jpn. **65**, 6 (1996); **65**, 1686 (1996).
[10] G. Z. Gershuni and E. M. Zhukhovitskii, *Convective Stability of Incompressible Fluids*, Israel Program for Scientific Trans-

lations, Jerusalem, 1976.
[11] D. T. J. Hurle, E. Jackman, and C. P. Johnson, J. Fluid Mech. **64**, 565 (1974).
[12] A. E. Gill, J. Fluid Mech. **65**, 209 (1974).
[13] J. E. Hart, J. Fluid Mech. **132**, 271 (1983); Int. J. Heat Mass Transf. **26**, 7 (1983).
[14] P. Laure and B. Roux, C. R. Acad. Sci., Ser. II: Mec., Phys., Chim., Sci. Terre Univers **305**, 1137 (1987).
[15] H. P. Kuo and S. A. Korpela, Phys. Fluids **31**, 33 (1988).
[16] E. Drummond and S. A. Korpela, J. Fluid Mech. **182**, 543 (1987).
[17] W. Schopf and O. Stiller, Phys. Rev. Lett. **79**, 22 (1997); **79**, 4373 (1997).
[18] R. Delgado-Buscalioni and E. Crespo del Arco, Int. J. Heat Mass Transf. **42**, 2811 (1999).
[19] A. C. Skeldon, D. S. Riley, and K. A. Cliffe, J. Cryst. Growth **162**, 96 (1996).
[20] D. Henry and M. Buffat, J. Fluid Mech. **374**, 145 (1998).
[21] R. Delgado-Buscalioni, E. Crespo del Arco, and P. Bontoux, Eur. J. Fluid Mech. (to be published).
[22] M. Braunsfurth and T. Mullin, J. Fluid Mech. **327**, 199 (1996).
[23] K. E. McKell, D. S. Broomhead, R. Hones, and D. T. J. Hurle, Europhys. Lett. **12**, 513 (1990).
[24] L. Davoust, R. Moreau, and R. Bolcato, Eur. J. Mech. B/Fluids **18**, 621 (1999).
[25] R. Delgado-Buscalioni, Ph.D. dissertation, UNED, Madrid, 1999.
[26] A. Bejan and C. L. Tien, J. Heat Transfer **100**, 641 (1978).
[27] S. A. Nikitin, D. S. Pavlowskii, and V. I. Polezhaev, Fluid Dyn. **31**, 4 (1996); **31**, 503 (1996).
[28] M. Braunsfurth, A. C. Skeldon, A. Juel, T. Mullin, and D. S. Riley, J. Fluid Mech. **342**, 295 (1997).
[29] R. Delgado-Buscalioni *et al.*, C. R. Acad. Sci., Ser. IIb: Mec., Phys., Chim., Astron. **36**, 711 (1998).
[30] J. M. Vanel, R. Peyret, and P. Bontoux, in *Numerical Methods for Fluid Dynamics II*, edited by K. W. Morton and M. J. Baines (Clarendon Press, Oxford, 1986), pp. 463–475.
[31] R. I. Issa, B. Ahmadi-Befrui, K. R. Beshai, and A. D. Gosman, J. Comput. Phys. **93**, 388 (1991).